Numerical studies of transport and anisotropic exchange interaction in InAs nanowires

by

Nupur Gupta

A thesis
presented to the University of Waterloo
in fulfillment of the
thesis requirement for the degree of
Master of Science
in
Physics - Quantum Information

Waterloo, Ontario, Canada, 2012

I hereby declare that I am the sole author of this thesis. This is a true copy of the thesis, including any required final revisions, as accepted by my examiners.

I understand that my thesis may be made electronically available to the public.

Authorship Statement

The contents of Chapter two are based on a collaboration, and in particular the preprint:

- Gupta, Nupur, Yipu Song, Gregory W. Holloway, Urbasi Sinha, Chris Haapamaki, Ray R. LaPierre, and Jonathan Baugh. "Temperature-dependent electron mobility in InAs nanowires." arXiv preprint arXiv:1210.3665 (2012).

with the manuscript largely prepared by Jonathan Baugh. Passages have been adapted for inclusion here with his consent. In particular, the nanowires used in the study were prepared at McMaster univeristy by Chris Haapamaki and Ray LaPierre. The experimental measurements and extraction of mobility presented in Section 2.1 was performed by Y. Song and G. Holloway. The numerical models discussed in Section 2.2 and Section 2.3 were developed by myself. The concept of correlated scattering presented in Section 2.4 was developed primarily by J. Baugh, the results presented therein are my own.

The contents of Chapter three are based on a collaboration with Kaveh Gharavi and Jonathan Baugh, for which the manuscript was jointly prepared by K. Gharavi, myself and benefitted from editing by J. Baugh. Passages have been included here with the consent of co-authors. In particular, the device model presented in Section 3.1 was developed by myself. Methods A and C in section 3.2 were proposed by myself, methods B and D were proposed by J. Baugh. The results discussed in Section 3.3 are my own; the presentation benefitted from the work of co-authors. The modified qubit encoding proposed in Section 3.4 is based on discussions with Stefano Chesi.

Abstract

High spin-orbit coupling and low effective mass of electrons in InAs nanowires makes it an attractive material for studying quantum physics in mesoscopic and nanoscale quantum devices. We first study the transport properties of FET devices made of InAs nanowires of diameter in the range of 35-70 nm. The temperature dependence of electron mobility in InAs nanowires from 10-200 K exhibits a positive slope below approximately 40 K, then turns over to a negative slope at higher temperatures. This is explained by Coulomb scattering from the surface donor like states that give rise to a subsurface accumulation layer and the thermal activation of these surface donors. The scattering rates are calculated using a momentum relaxation time approximation. The transition probabilities between the self-consistent Poisson-Schrödinger states of a 50 nm diameter nanowire are calculated using Fermi's golden rule. The results clarify the dominant scattering mechanism in InAs nanowires and signify the need for surface passivation to obtain high mobility devices. In a second study, we model a gate defined double quantum dot in the nanowire with high spin-orbit coupling in order to determine the precise gate voltage dependence of the exchange Hamiltonian. This modelling is critical for designing two-qubit quantum logic operations in the nanowire double dot architecture. A quantum double well structure is simulated based on the realistic potential created by a set of fine local electrostatic gates in the presence of nanowire surface accumulation layer. An effective spin Hamiltonian is derived for a pair of interacting electrons localized in the double dot system in the presence of a strong spin-orbit coupling. The accuracy of the effective Hamiltonian is established by a strong agreement obtained between the dynamics generated by the effective Hamiltonian with those obtained by a numerically exact solution of the time-dependent Schrödinger equation. The parametric dependences of the effective exchange Hamiltonian on external magnetic field, barrier gate voltage, and spin-orbit field is determined. This opens the door to designing optimal pulses for high fidelity quantum gates in real InAs nanowire devices.

Acknowledgements

I would like to thank my supervisor, Dr. Jonathan Baugh, for his ideas and guidance that led to this work. I would like to thank my collaborators, Kaveh Gharavi on the spin-orbit project, Greg Holloway and Yipu Song on the mobility project, and Jonathan Baugh on both. I would also like to acknowledge helpful discussions with Daryoush Shiri, Milad Khoshnegar and Stefano Chesi. I am thankful to the members of my committee for taking the time to read the thesis and providing feedback in committee meetings.

Table of Contents

List of Figures

Chapter 1

Introduction

Semiconducting nanowires as building blocks in bottom-up nanoelectronics provide a rich field of opportunity for studying quantum phenomena in nanoscale devices. This advantage is afforded by the nanowire geometry approaching one dimensionality which allows for large scale fabrication of coupled nanoscale circuits. The choice of Indium Arsenide (InAs) as the semiconductor material further supplements this advantage due to, a) small effective mass of electron $m^* = 0.023m_e$ that leads to, i) stronger quantum confinement, giving wider separation of the high energy states in InAs quantum dot spectrum from the low lying subspace which is the regime of interest for quantum information applications, ii) high electronic mobility relevant for charge transport based electronic devices, b) large and tunable Landé g factor [1, 2] and spin-orbit (SO) coupling [3] that allows for efficient control over the electronic spin degree of freedom for use in spintronic devices. The nanowires we investigate are grown in a gas source molecular beam epitaxy (GS-MBE) system through vapour-liquid-solid (VLS) growth method using a gold catalyst particle. The nanowire diameter is determined by the size of the Au seed particle while the length is determined by the growth time. The nanowires are integrated into a field-effect transistor (FET) device through a series of nano-lithographic steps. A FET is a three-terminal device configured like a parallel plate capacitor. The charge density in the device can be controlled (down to zero) with global or local gates. The tuning of charge to a single electron in an electrostatically defined quantum dot as well as the electron-electron coupling between adjacently fabricated quantum dots has been demonstrated in 50-100 nm nanowires by selective depletion of electrons through local electrostatic gates [4, 5].

In this thesis, we address problems that have the end goal of effecting a spin based prototype quantum information processor (QIP) realized in InAs semi-conductor nanowires. The objective is to fully control quantum mechanical processes at the single electron level in a way that adheres to all of the criteria required for quantum bits (qubits). In 2000 David DiVincenzo outlined a set of principles that would guide the physical design of a device capable of performing quantum computation [6]. The guidelines are the following:

1. Well-characterized qubits: Identify a two-level quantum property of a scalable system within which to encode the qubit. The internal and control Hamiltonians of the system should be known accurately.

2. Initialization: It must be possible to prepare the system in a known state at the start of the computation.

3. Decoherence: The loss of information in the quantum state resulting from unwanted interactions with the environment are to be limited below the error thresholds of fault tolerant quantum computation [7, 8, 9].

4. Universal set of gates: It should be feasible to perform an arbitrary unitary transformation of a given initial state to any coherent state in the Hilbert space of the system. This requirement is equivalently expressed as the ability to perform an arbitrary single spin rotation and an entangling two spin operation such as a controlled NOT gate [10].

5. Measurement: It must be possible to perform quantum measurement on a single or multiple qubit state which is the output of quantum computation.

The idea of electron spin qubits localized in an array of adjacent quantum wells was proposed as early as 1998 [11, 12], encouraged also by the prospects of studying controlled non-equilibrium spin dynamics of magnetic nanosystems. In the following, we outline the generalized framework proposed in [11, 12] for performing quantum computation in electrostatically gated quantum dots. The initial state of the system corresponds to the well-separated regime of the two quantum dots occupied by a single electron each. The spin states are initialized by letting the system evolve to its thermal ground state at sufficiently low temperature in the presence of a strong Zeeman field, $E_Z >> k_B T$ where E_Z is the Zeeman energy gap between up and down spin states, kT is the thermal energy at temperature T. The control required for performing single qubit gates, which in this case amounts to an arbitrary rotation of a single spin, is provided by local time-dependent magnetic fields. Interactions between individual spin qubits are facilitated by lowering the height of tunneling potential barrier separating the two electrons. The resulting *exchange interaction* allows for fast and electrostatically tunable two qubit gates, $t \sim 350$ ps [13]. As the final step, a projective measurement of the two electron spin in singlet-triplet basis is achieved through the Pauli spin blockade [13].

This design was originally restricted to the material systems where the electron's spin and orbital degrees of freedom coupled weakly enough to have negligible effects on spin dynamics. An intrinsic spin-orbit (SO) interaction arises in atomic physics, when an orbiting electron is subjected to a nuclear electric field which in the electron's rest frame is Lorentz transformed into an effective magnetic field acting on its spin. The form of SO Hamiltonian as a first order relativistic correction to a single electron Schrödinger equation

is:

$$H_{SO} = \frac{\hbar}{4m^2c^2}\boldsymbol{\sigma}.(\boldsymbol{p} \times \nabla V) \tag{1.1}$$

where m is the electron mass, c is the speed of light, $\boldsymbol{\sigma}$ are the Pauli spin matrices, $\boldsymbol{p}$ is the momentum vector, and ∇V is the gradient of the electrostatic potential. The SO coupling in crystalline structures arises from the interaction of conduction electrons with the lattice potential. There are two contributions to the SO Hamiltonian in crystalline low-dimensional systems. A Dresselhaus component [14] arises from the bulk inversion asymmetry (BIA) of underlying Wurtzite [15] crystal structure that is exhibited in the nanowires of interest to us. An additional Rashba component [16] results from the structure inversion asymmetry (SIA) of the confining potential.

While the actual value of spin-orbit coupling parameter in a localized quantum dot is subject to the details of local electric fields, an order of magnitude estimate is provided by direct experimental observations [17, 18]. The presence of SO interaction was detected experimentally by measuring the size of an avoided crossing in double quantum dot at the transition from singlet to triplet ground state in a varying magnetic field. This anti-crossing results from the SO induced mixing of singlet and triplet spin states. The size of the anticrossing was measured to be $\Delta_{SO} = 0.23$ meV in a quantum dot of lateral dimension $\lambda = 23$ nm in 50 nm diameter InAs nanowires [17]. An intuitive measure of SO interaction is given by SO length $\lambda_{SO} = 127$ nm corresponding to the Δ_{SO} above. The SO length is the distance traveled through which the electron spin is rotated by an angle of π. In general, SO interaction in InAs nanowires is calculated to be two orders of magnitude higher than in GaAs [18]. At such high values, spin orbit Hamiltonian H_{SO} can no longer be treated as perturbative correction to the system Hamiltonian.

In fact, H_{SO} has found an application in QIP as an efficient control handle for single spin manipulations. The time-dependent electrical control of an electron's orbital motion is translated into a time-dependent magnetic field which acts on the electron spin and consequently induces spin precession in a process termed electrically detected spin resonance (EDSR) [19]. In the absence of SO coupling, large amplitude microwave magnetic fields are required for performing fast single electron rotations, which is associated with a lossy process of photon assisted tunneling of the electron out of the dot. The EDSR replaces the practically limiting requirement of localized strong Zeeman coupling with an AC electric field for manipulation of single electron spins. This motivated our choice of material in the present work. Electrically controlled coherent single spin rotations have been demonstrated in GaAs [20] as well as in InAs [21].

On the other hand, the SO interaction disturbs the isotropic structure of effective spin Hamiltonian for a pair of coupled spins described by the so called *Heisenberg exchange interaction* [22]. The exchange interaction between the coupled spins enables entangling dynamics necessary for generating universal quantum gates [11, 23]. The effective spin interaction between an electron pair on restriction to the lowest spatial states of the system is completely described by an isotropic exchange interaction $H_{ex} = J\boldsymbol{\sigma}_1.\boldsymbol{\sigma}_2$, where J is the

strength of exchange coupling, and $\boldsymbol{\sigma_i}, i = 1, 2$ is the spin operator for each electron. The strength of the exchange interaction J varies with the height of the interdot tunneling barrier. Under the assumption that the barrier gating action is adiabatic, the unitary resulting fromevolving under the exchange interaction is $U = e^{-i\int_0^t J(t').dt'\boldsymbol{\sigma}_1.\boldsymbol{\sigma}_2}$, where t is the time during which the spin interactions are turned on via tunneling. A straightforward construction of a SWAP[1] operation results from U when the exchange is pulsed in a manner such that $\int_0^t J(t').dt' = \pi$. A desirable two-qubit gate, the controlled-NOT[2] gate, is then designed by combining two $\sqrt{SWAP}$ operations ($\int_0^t J(t').dt' = \pi/2$) with single spin rotations in a well-defined sequence. The coherent control of coupled spins was performed in asymmetric double quantum dots created in GaAs/AlGaAs heterostructures by Petta et al. [13]. Rabi oscillations were measured between $S_0 - T_0$ spin states evolving under the exchange interaction in the presence of a detuning $\epsilon \propto V_L - V_R$ between the two quantum dots, where tunnel barriers $V_{L,R}$ connect each dot to the adjacent reservoirs, allowing electrons to be transferred into the dots. A schematic of their experiment is shown in figure 1.1. The ability to perform single qubit rotations along with the controlled-NOT gate guarantees the implementation of an arbitrary unitary operation on the two-qubit (two-spin) Hilbert space. In other words, these gates form a universal gate set for quantum computation [10]. However, in the presence of SO coupling, a non-zero matrix element $\Delta = \langle S_0|H_{SO}|T_\pm\rangle$ arises leading to mixing between singlets and triplets. Additional spin structure arises in the effective spin Hamiltonian leading to the following general form: an isotropic exchange term proportional to J' (here J' in the general case is distinguished from the isotropic exchange strength J in the absence of SO coupling), a Dzyaloshinskii-Moriya term proportional to $\boldsymbol{\beta}$ which is first order in SO coupling, and a second order pseudo-diploar term proportional to unitless scalar γ [24, 25]:

$$H_{spin} = J'(\boldsymbol{\sigma}_1.\boldsymbol{\sigma}_2 + \boldsymbol{\beta}.(\boldsymbol{\sigma}_1 \times \boldsymbol{\sigma}_2) + \gamma(\boldsymbol{\beta}.\boldsymbol{\sigma}_1)(\boldsymbol{\beta}.\boldsymbol{\sigma}_2)). \tag{1.2}$$

The exchange coefficients J', $\boldsymbol{\beta}$ and γ depend on the double well potential profile and the external magnetic field. This SO induced anisotropic exchange interaction in coupled double quantum dots was first highlighted by Kavokin [24] as a non-negligible source of error in a semiconductor solid state based quantum information processor; the strength of anisotropic terms relative to the isotropic exchange interaction was estimated to be $\delta \sim 10^{-1} - 10^{-2}$. This corresponds to an error rate $p_e \approx \delta^2$ larger than the current thresholds for fault tolerant computing, $p_e(th) \approx 10^{-5}$ [26]. The SO coupling strength is two orders of magnitude higher in InAs. Newer studies considered SO induced terms in the effective spin Hamiltonian both as an error source to be mitigated [27, 28] and a useful tool for designing more general quantum gates [29]. In both cases, precise knowledge of the SO Hamiltonian is crucial for engineering high fidelity gates. Motivated by this, Baruffa et al. [30] developed analytical formulations of the effective spin Hamiltonian under the

[1]SWAP gate interchanges the states of two spins (qubits).

[2]C-NOT is an entangling two qubit gate which flips the state of a 'target' qubit depending on the state of a 'control' qubit which remains unaffected.

assumption of a weak spin-orbit coupling with reference to GaAs quantum dots. In this thesis, we extend their analysis to include a strong spin-orbit interaction appropriate for InAs. We present a numerical study of a realistically gated double well system treating spin-orbit coupling on equal footing with other terms in the Hamiltonian. Further, we identify a pseudo-spin basis for encoding quantum information that emerges as the most suitable choice from the point of view of qubit preparation and manipulations.

In addition to the theoretical question of quantum gate design in the presence of a strong SO coupling described above, we address an experimental issue pertaining to the role of surface states in transport in nanowire FET devices which constitute the basic hardware of proposed spintronic quantum device. The high surface to volume ratio in nanowires renders the electron transport through the nanowire highly susceptible to surface physics. In particular, InAs has surface states that pin the Fermi level above the conduction band at the surface, unlike other III-V materials such as GaAs with larger band gap, in which similar surface states pin the surface Fermi level in the gap. These surface states act as electron donors and, therefore, lead to a surface accumulation layer [31]. In addition, random telegraph noise signals are measured in the nanowires resulting from charge trapping/detrapping due to defects in the oxide at the nanowire surface [32]. Together, the surface states and charge traps act as Coulomb scattering centers; the density of surface states is larger than that of charge traps and is expected to be a dominant contribution to scattering limiting the device performance. A second focus of this thesis is to understand and quantify the effect of donor-like surface states on electron transport which will provide a benchmark to compare with optimized nanowire devices in the future. In the next section, we outline in further detail the specific research problems addressed in this thesis and its organization.

1.1 Problem Description

The level of precision required for performing quantum operations in nanoscale physical devices warrants a detailed study of microscopic physical processes affecting the device operation. In the proposed nanowire qubit device, electron spins are localised in an externally gated double well potential profile created in the nanowire. The shape of this potential confines and controls the degree of interaction between the pair of spin qubits. An accurate knowledge of the spatial charge and potential distributions inside the nanowire is, therefore, highly desirable. We perform a study of electron mobility in InAs nanowires across a range of temperatures and voltages in a FET device. The experimental electron mobilities of the conduction electrons are indicative of the scattering mechanisms, which in turn sheds light on the underlying potential profile. The information obtained about the surface physics in the experimental study is utilized in the theoretical study of characterizing an effective spin Hamiltonian of a double quantum dot (DQD) system in the presence

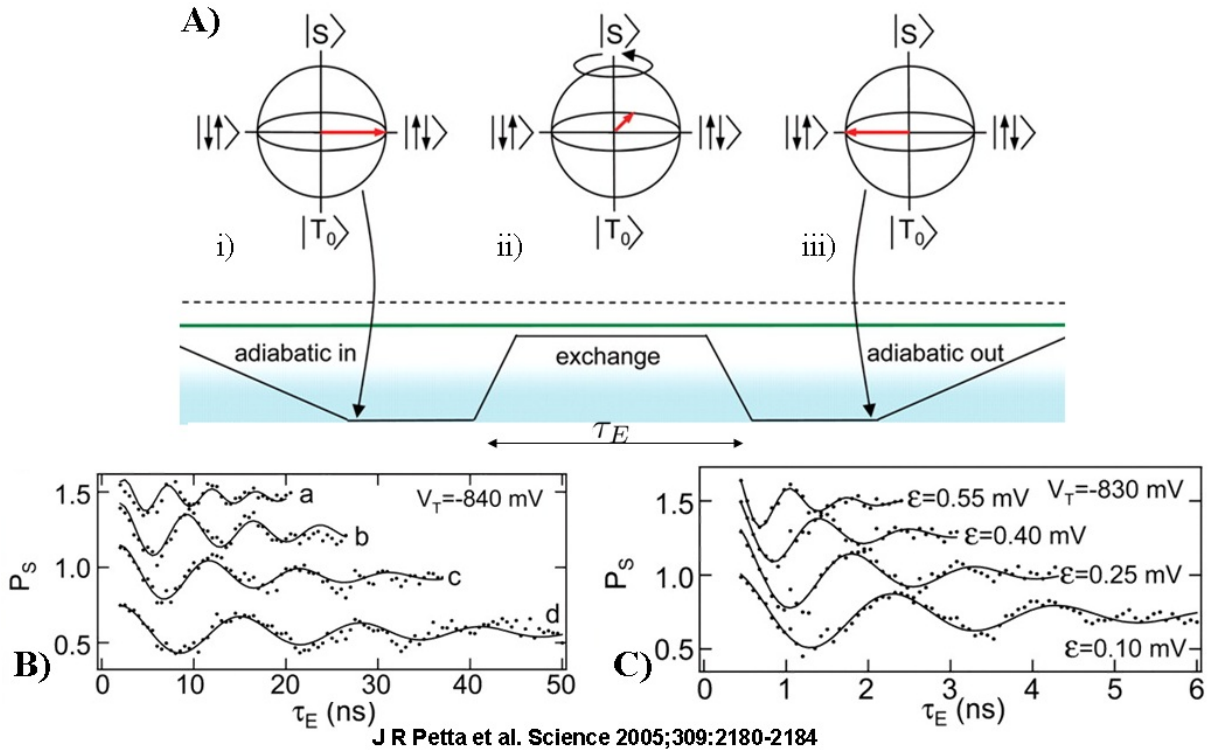

Figure 1.1: A) Bloch sphere for the $S_0 - T_0$ two level system that has $|S_0\rangle$ and $T_0\rangle$ at the north and south poles (z axis) and the states $|\uparrow\downarrow\rangle, |\downarrow\uparrow\rangle$ as the poles along the x axis. The system is initialized in the state $|\uparrow\downarrow\rangle$ marked by red arrow in i); application of a finite exchange $J(\epsilon)$ at detuning $\epsilon \propto V_R - V_L$ between the left and right quantum dots for time τ_E rotates the initial spin state about the z-axis of the Bloch sphere through an angle $\phi = J\tau_E/\hbar$ to a final state $|\downarrow\uparrow\rangle$ when $\phi = \pi$ as shown in iii). B) Plot of the singlet probability P_S as a function of time τ_E over several π cycles at an inter-dot tunnel coupling V_T for four different values of negative detuning ϵ labeled $a - d$, where detuning increases from a to d. A constant offset is applied to the plotted values for clarity. Faster Rabi oscillations were observed at smaller negative detuning. C) The time period of the oscillations was reduced by an order of magnitude on increasing the tunnel coupling controlled by V_T and by increasing detuning to positive values.

of spin-orbit coupling. The effective spin Hamiltonian would guide the experimental realization of coupled spin gates which are the building blocks of a universal gate set. In the next two sections, we summarize the two research problems that are the subject of this thesis.

1.1.1 Modelling Coulomb scattering to explain experimental mobility

The first problem addressed in this thesis pertains to the material properites of InAs nanowires. The theory of spin based quantum computation in InAs nanowires has been well laid out for nearly a decade now, and has helped accelerate advances in experimental solid state technology. However, new experimental challenges are born with the introduction of newer semiconducting materials in uncoventional geometries. An important mechanism which is detrimental to the operation of these devices is the presence of surface states that have been known to act as charged donor states and the presence of dynamical charge traps in surface oxide. We perform a numerical study of the role played by these surface states as scattering centers affecting the transport through the nanowires. The conductance measurements are taken for a set of device with nanometer radii from 35-70 nm over a temperature range of 20-200 K. Field effect mobility is then extracted from the slope of these conductance curves. Finite element modelling of charge and potential distribution under the influence of these charged surface states is performed under varying temperature and gate conditions. Calculation of scattering rates from these charged surface states are found to provide a very close match to the scale and temperature dependence of experimentally observed mobilities. This study emphasizes the need for tailored surface passivation of the future nanowire devices, in order that they are capable of realizing stable quantum dots. Furthermore, the complete characterization of the transport in nanowire devices provides a benchmark to compare with the improved devices in future such as core-shell nanowires [33]. In Chapter two, we first present the conductance and field-effect mobility measurements for nanowire FET devices of diameter (35, 50, 75) nm. In section 2.2, we discuss the finite element method (FEM) simulation of nanowire charge and potential profile obtained from a self-consistent Poisson-Schrödinger solver. In section 2.3, we describe the calculation of scattering rates in momentum relaxation time approximation using Fermi's golden rule and compare the results with the experimental study in section 2.3.1. The results are summarized in section 2.4.

1.1.2 Modelling exchange Hamiltonian for designing two qubit quantum gates

Double quantum dots are considered a model system for qubits in spin based solid state quantum computation schemes. An electrostatically gated nanowire device is an attractive physical system within which to realize such qubits. The high spin-orbit coupling in InAs provide an efficient route to performing single qubit operations through EDSR while fast control of the exchange interaction allows coherent manipulation of coupled spin qubits.

We identify a theoretical challenge in that the high SO coupling disturbs the conventional design of two qubit coupled gates such as SWAP, controlled-NOT gate which are the building blocks for a universal gate set. To overcome this challenge, we first develop an effective spin Hamiltonian description of the exchange interaction between electrons spins in a realistic nanowire double quantum dot geometry. This is achieved by projection of the complete Hilbert space solutions of the double dot system in the presence of spin-orbit coupling to a 4-dimensional subspace of two-electron spins. Such an effective spin Hamiltonian description paves way for utilizing the exchange interaction to design quantum gates, however, the resulting gates will only be as accurate as the underlying Hamiltonian. It is, therefore, important to also benchmark the accuracy of derived spin Hamiltonians. We achieve this through an exact comparison of the dynamics generated by this Hamiltonian with those obtained from the exact solution of the time dependent Schrödinger equation. Further, we characterize the dependence of effective spin Hamiltonian on experimental control parameters - double well barrier height, external Zeeman coupling and spin-orbit field. The large spin-orbit coupling in InAs also poses a challenge for the preparation of pure spin states to be used as qubits due to the presence of non-trivial spin space correlations in the system. This problem is mitigated by choosing the basis of spin-orbit eigenstates in the limit of weak interdot coupling as the basis for representing logical qubits. Towards this end, a revised procedure for calculating effective spin Hamiltonian is outlined and constitutes ongoing work. The problems described above are considered in detail in Chapter three. A finite element model for a gated InAs nanowire double dot is described in Sec 3.1. In Sec 3.2, we describe in detail the numerical methods for obtaining the double well potential profile and calculating the time evolution of the system. We then discuss several approaches for deriving H_{spin} from the numerical results. In Sec 3.3, we analyze the accuracy of H_{spin} in describing the dynamics, and present results on the parametric dependence of H_{spin} on the barrier gate voltage, the external magnetic field, and the spin-orbit field. In Sec 3.4, we examine the appropriate pseudo-spin basis for encoding quantum information in the system. Finally, we summarize and discuss the results in Sec 3.5.

A summary of the main results of the thesis and directions for future work are presented in Chapter four. The details of the numerical solvers employed in this work are available in Appendix B.

Chapter 2

Surface Scattering and Transport

Electron transport in nanowires is marked by a pronounced interaction of carrier electrons with the surface. In addition to surface roughness, the presence of charged defects, impurities at surface, amplifies the role of electron-surface interaction in transport. Although it is widely believed that surface layer plays a dominant role in nanowire transport [49, 50, 51, 52], a detailed study of the dominant scattering mechanism has been missing. In this chapter, we develop finite element method (FEM) based numerical procedures for modelling charge and potential distribution in a globally back-gated gated InAs nanowire FET device. The numerical model is employed to explain a characteristic temperature-dependent mobility behavior seen in multiple FET devices fabricated from InAs nanowires of different diameters. Electron mobilities are seen to rise with temperature peaking at $3,000 - 20,000\,\mathrm{cm}^2 V^{-1} s^{-1}$ at $T \approx 40$ K followed by a nearly monotonic decrease with temperature up to $T = 200$ K. These mobilities are too low to be limited by optical or acoustic phonon scattering, which yield estimated bulk mobilities 2-3 orders of magnitude larger than those observed here [48]. This is expected to remain true even in quasi-one-dimensional systems, where phonon scattering is moderately enhanced due to a larger available phase space for scattering [54]. Surface states are known to be present in InAs nanowires at densities $\sim 10^{11} - 10^{12}\,\mathrm{cm}^{-2}\,\mathrm{eV}^{-1}$ and to act as donors. These positive donor like states result from the pinning of Fermi level above the conduction band at nanowire surface, and are the source of majority carriers in the nanowire. We argue that a sufficient density of these positively charged surface states should be more effective at scattering electrons than surface roughness, and therefore limit the mobility. Chemical treatment of the nanowire surface is seen to have a strong effect on the temperature-dependent mobility consistent with the hypothesis of surface dominating the transport.

The collisions of electron with Coulomb impurities are treated in a modified Born approximation in the calculation of scattering rates. A scattering potential resulting from a random distribution of impurities along the nanowire surface is simulated using the numerical model. We assume a temperature dependent ionization of donor states in the model. This is related to the experimental observations of shifts in threshold voltage of

the conductance vs gate voltage curves with temperature across a range of 20-200 K. We find that the decrease in mobility with temperature above ~ 50 K can only arise from an increase in the number of ionized surface states. A minor contribution to the decrease of mobility with temperature comes from populating higher radial subbands with increasing temperature which pushes the electron density closer to the surface, but it is not alone found to be sufficient to cause a negative slope in the mobility versus temperature.

Theoretical model developed here provides good agreement with the experiments and also plays an essential role in understanding the quantum size effect and surface scattering in these nanowire devices. The results underscore the need for tailored surface passivation techniques to reduce the density of surface scatterers and smooth the local electronic potential, leading to increased carrier mobility and cleaner devices for a wide range of quantum transport and optoelectronics applications. Further, the results obtained for pure InAs nanowires serve as a benchmark to compare with the future studies of passivated nanowires.

Monocrystalline InAs nanowires were grown in a catalytically driven epitaxial process by Christopher Haapamaki and Ray LaPierre at McMaster University. Details of the growth process are included as they are relevant for the study of scattering in nanowires. Fabrication of nanowire FET devices and experimental measurements of conductance presented in section 2.1 were performed by Yipu Song and Greg Holloway. In Sec. 2.2 we provide details on the numerical finite element method (FEM) model used to simulate charge and potential distribution in the nanowire. In Sec. 2.3 we discuss the framework for calculating remote impurity scattering from charged surface states. The summary and conclusions are presented in Sec. 2.4.

2.1 Experimental measurements of mobility in field-effect transistors

InAs nanowires were grown in a gas source molecular beam epitaxy (GS-MBE) system using Au seed particles. A 1 nm Au film is heated to form nanoparticles on a GaAs (111)B substrate. For nanowire growth, In atoms were supplied as monomers from an effusion cell, and As_2 dimers were supplied from an AsH_3 gas cracker. The nanowires grew in random orientations with respect to the GaAs (111)B substrate, possibly due to the large lattice mismatch strain between InAs and GaAs. Transmission electron microscopy (TEM) analysis, shown in figure 3.1a, indicated a Au nanoparticle at the end of each nanowire (darker contrast at the left end), consistent with the VLS process. Most nanowires had a rod-shaped morphology with negligible tapering and a diameter ($\sim 20 - 80$ nm) that was roughly equal to the Au nanoparticle diameter at the top of each nanowire, indicating minimal sidewall deposition.

A common occurrence in III-V nanowires is the existence of stacking faults whereby the crystal structure alternates between zincblende and wurtzite, or exhibits twinning, along

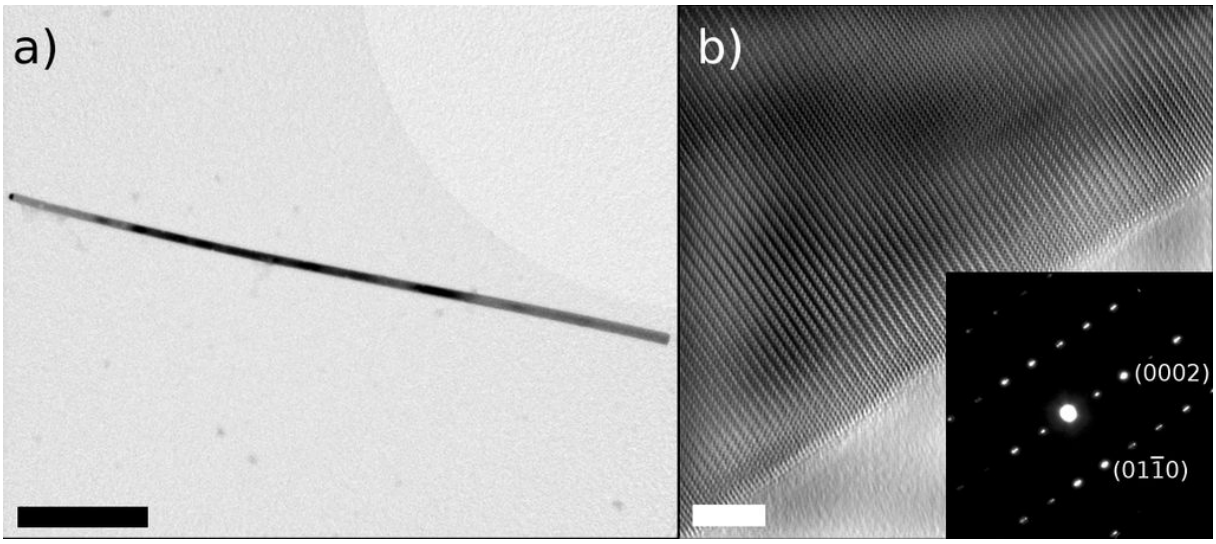

Figure 2.1: (a) Low and (b) high magnification bright-field TEM images of an InAs nanowire grown by GS-MBE at 0.5 μm/hr. Scale bars are 500 nm in (a) and 5nm in (b). The inset in (b) shows selected area diffraction pattern along the $[2\bar{1}\bar{1}0]$ zone axis indicating pure wurtzite crystal structure. A majority of wires grown under these conditions had low stacking fault densities < 1 μm^{-1}.

the nanowire length. It has been shown that growth parameters in metalorganic chemical vapour deposition (MOCVD) have profound effects on the InAs nanowire crystal phase [36, 37]. Zincblende, wurtzite, or mixed zincblende/wurtzite nanowires were formed by simply tuning the temperature and V/III flux ratio. It was found that for GS-MBE grown InAs nanowires, stacking faults can be nearly eliminated and pure wurtzite structures can be realized at sufficiently low growth rate $\sim 0.5\mu$m/hr. At higher growth rates, but otherwise identical growth conditions, the InAs nanowires exhibited a much larger fraction of stacking faults on average. For example, TEM analysis of InAs nanowires grown at a rate of 1μm hr^{-1} exhibited an average linear density of stacking faults ≈ 1 μm^{-1}. The density of faults was found to diminish dramatically when the growth rate was reduced. Selected area electron diffraction for a typical nanowire (inset of figure 3.1b) confirms the pure wurtzite crystal structure and the absence of stacking faults.

Field-effect transistors (FETs) were fabricated by mechanically depositing as-grown nanowires on a 175 nm thick SiO_2 layer above a n^{++}-Si substrate that functions as a back-gate, and writing source/drain contacts for selected wires using electron-beam lithography. This was followed by an etching / chemical passivation process to remove the native oxide and prevent regrowth [41] prior to evaporation of Ni/Au contacts. Channel lengths ranged from 0.7 - 3 μm. Transport measurements were carried out in He vapour in an Oxford continuous flow cryostat operating from 4 K to room temperature. Bias and gate voltages were applied using a high resolution home-built voltage source, and a DL Instruments current preamplifier was used to measure DC current at a noise floor ~ 0.5 pA/$\sqrt{Hz}$.

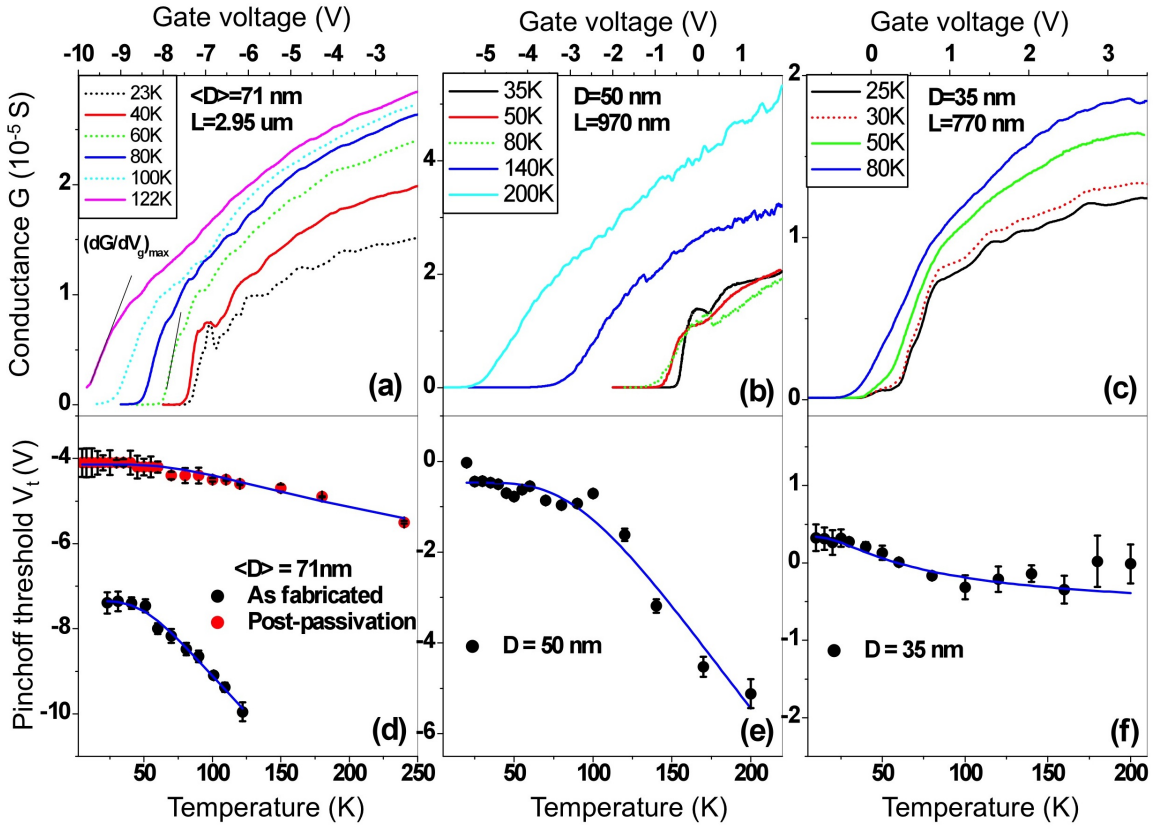

Figure 2.2: (a-c) Conductance pinchoff curves for devices $1-3$ at selected temperatures. D is the nanowire diameter and L the FET channel length (device 1 is tapered with an average nanowire diameter $\langle D \rangle = 71$ nm). The tangent lines drawn on the $T = 122$ K and $T = 60$ K traces in (a) indicate the maximum slopes corresponding to peak field-effect mobility. The pinchoff threshold voltage is defined as the intercept between this tangent line and the $G = 0$ axis. (d-f) The pinchoff threshold voltages versus temperature extracted from the conductance measurements. In (d), data are shown for device 1 before and after an ammonium polysulfide etching / passivation process is applied to the FET channel (the data in (a) correspond to the as-fabricated case). The empirical fits in (d-f) are of the form $V_t = V_0 + V_1 e^{-E_a/kT}$ as described in the text.

All devices tested at room temperature displayed fully Ohmic I-V characteristics, with resistances typically in the range of $5-100$ kΩ.

Many such devices were investigated to varying levels of detail, and gave qualitatively similar results. Here we will focus on three representative devices, denoted 1, 2 and 3 with nanowire diameters D=71, 50 and 35 nm, respectively. Devices 2 and 3 had untapered nanowires, whereas the device 1 nanowire was tapered with diameter linearly varying from

53 nm to 90 nm ($\langle D \rangle$=71nm) across the FET channel. Device 2 is used as the basis for all model simulations described below. The data from device 1 (tapered nanowire) is included because it was the highest mobility device of this set, the temperature dependence of its mobility followed a similar trend to the untapered devices, and it was one of three devices for which post-measurement TEM analysis was performed.

Figure 2.2(a-c) shows conductance $G = I/V_{sd}$, where I is current and V_{sd} is source/drain bias, versus backgate voltage for devices 1–3 at selected temperatures, at a bias $V_{sd} = 1$ mV. For all three devices, the maximum transconductance $\left(\frac{dG}{dV_g}\right)_{max}$ is seen to decrease as temperature is raised above $\sim$ 30K. Figure 2.2(d-f) show the pinchoff threshold voltages V_t corresponding to the data in figure 2.2(a-c), where V_t is defined as the intercept between the tangent line of maximum slope and the $G = 0$ axis. V_t typically shifts toward more positive gate voltages as temperature is decreased, and saturates below $\sim$ 50 K. Note that all temperature sweeps reported here were from low to high temperature. We fit the pinchoff threshold data to an empirical function based on thermal activation $V_t = V_0 + V_1 e^{-E_a/kT}$, where k is Boltzmann's constant, typically yielding an $E_a \sim 15 - 30$ meV. The fits to some devices, however, showed smaller E_a such as for device 3 in figure 2.2f, with an $E_a \approx 5$ meV. Note that for device 1 in figure 2.2d we also plot the V_t measured after an ammonium polysulfide etching/passivation process was applied to the FET channel (labeled 'post-passivation'). Interestingly, V_t shifted considerably to more positive gate voltage post-passivation, and also showed much weaker temperature dependence. This suggests that the as-grown nanowires in this study may have a relatively large density of surface states acting as electron donors, and that this density is reduced by sulfur passivation, as has been previously noted [46]. Indeed, for some as-grown nanowire FET devices in the diameter range $50-70$ nm we were not able to see significant gating effect at room temperature, and in some cases, even at low temperature. We have also observed, for some nanowires, significant shifts in V_t after annealing in vacuum at 80°C, which indicates that gas adsorbates in ambient conditions can strongly affect the nanowire surface potential [39].

From the measured conductance versus backgate voltage curves, both the field-effect mobility and the effective mobility [42] may be extracted. The field-effect mobility is a lower bound on the effective mobility, and is defined as

$$\mu_{fe} = q^{-1}\frac{d\sigma}{dn} = \frac{L}{C'_g}\frac{dG}{dV_g}, \tag{2.1}$$

where σ is conductivity, n is the electron concentration, q is electron charge, C'_g is the gate capacitance per unit length (see Methods). Equation 2.1 only strictly holds at peak mobility, where $\frac{d\mu_{fe}}{dn} = 0$. The effective mobility is defined as

$$\mu_{eff} = \frac{LG}{C'_g(V_g - V_t)}, \tag{2.2}$$

where V_t is the pinchoff threshold voltage defined previously, and the condition $V_{sd} << V_g - V_t$ must be satisfied. The field-effect and effective mobilities for the same conductance

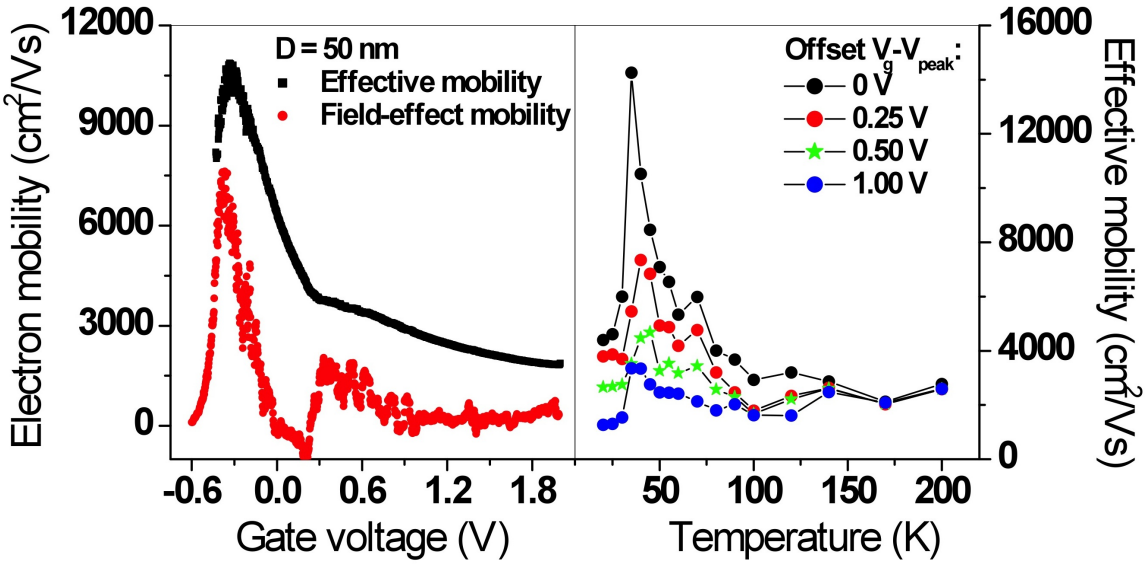

Figure 2.3: (left) Comparison of the field-effect and effective mobilities for device 2 at $T = 40$ K. (right) The temperature dependence of effective mobility for device 2 at different values of gate voltage relative to V_p, the gate voltage at which peak mobility occurs. The values at V_p are shown by black dots, at $V_p + 0.25$ V by red dots, etc. The mobility at $V_p + 0.5$ V is typically just at the crossover point between the two slopes than can be seen in the effective mobility in the left panel.

data at $T = 40$ K (device 2) are compared in figure 2.3. The effective mobility is typically a smoother function of V_g than μ_{fe}, and $\mu_{eff} \geq \mu_{fe}$ for all of our data. Two regimes can be clearly seen in μ_{eff}: $|\frac{d\mu_{eff}}{dV_g}|$ is larger from $V_g = -0.25V$ to $V_g = +0.25V$ than it is at more positive gate voltages. In figure 2.3 we show the effective mobility versus temperature for this device for different values of gate voltage relative to the position (V_{peak}) of peak effective mobility. The data shown are for the gate voltage at $V_{peak} + \delta$, where the top curve (black dots) is for $\delta = 0$, and the lower curves (red, green, blue) are for $\delta = 0.25, 0.5, 1.0$ V, respectively. The temperature dependence is most pronounced at peak mobility, but follows a similar trend for points on the high slope region of the effective mobility curve. For mobilities at large positive gate voltages relative to V_{peak}, the temperature dependence becomes negligible.

A qualitatively similar temperature dependence is observed for the other two devices as shown in figure 2.4. At a given temperature, the mobility increases with nanowire diameter, as was reported previously [42]. This is consistent with the mobility being dominated by surface charge scattering, as the overlap of the carrier distribution with the scattering potential becomes much stronger at smaller diameters [55]. Motivated by this hypothesis, the mobility vs temperature data for the three devices was fit to empirical function of the

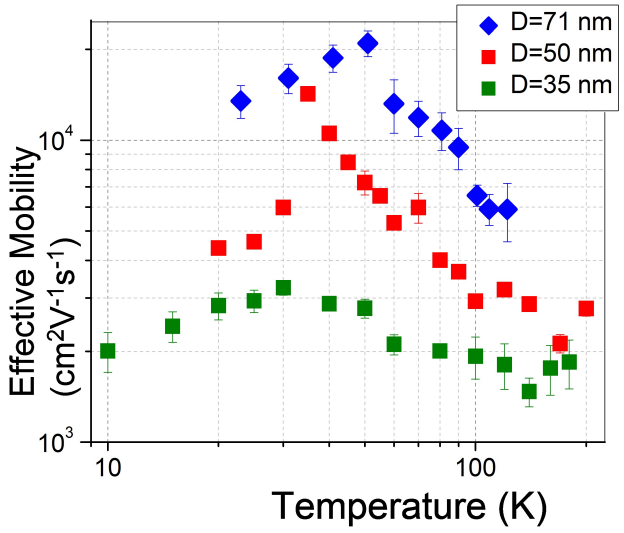

Figure 2.4: Experimental peak effective mobilities versus temperature for devices 1-3 plotted on a log scale. The mobilities show an increase with nanowire diameter. The highest mobility seen is $\mu_{eff} = 20,964\,\mathrm{cm}^2V^{-1}s^{-1}$ in D=71 nm device at T=51 K.

form $\mu(T) \propto T^x N(T)^{-y}$, where $N(T)$ is the number of surface scatterers, approximated as $N(T) \propto (1 + Be^{-E_a/kT})$ and found to yield a good agreement with $y = 2$ and $x \sim 1$. This function is based on the the following reasoning. For a fixed number of scatterers, the average mobility increases with temperature as T^x, where $x \sim 1$, since the carrier concentration increases with temperature leading to an increase in the Fermi velocity, which reduces the scattering probability [55, 47]. On the other hand, an increase in the number of scatterers decreases mobility. In the limit of a low density of scatterers and a high probability of scattering per defect, scattering events can be treated as uncorrelated, and $\mu \propto N^{-1}$. However, for scattering from surface states, there is a high density of scatterers with a low probability of scattering per defect, leading to correlated scattering [56] (see details in results section). Here, the electron wavefunction remains coherent while interacting with multiple surface charges simultaneously, which leads roughly to $\mu \propto N^{-2}$, since the scattering matrix element is roughly proportional to N, so the transition rate is proportional to N^2. The intuition developed here is used in the first-principles calculation of scattering rates presented in the results section.

2.2 Numerical modeling of field-effect transistors

The nanowire transistor was simulated using a finite-element method implemented in the COMSOL® multiphysics package. The model consisted of a $L = 1\mu$m long, $D = 50$ nm

diameter nanowire atop a 175 nm thick SiO_2 layer above a conducting layer serving as a backgate. Due to the low effective mass of electrons in InAs, it is essential to use a self-consistent Poisson-Schrödinger solver [57] so that quantum confinement is properly taken into account. The intrinsic carrier concentration of electrons and holes in InAs is much lower than the observed density of ionized surface donor states [31] in the temperature range of interest and is neglected. The model assumes that the conduction electron concentration at zero gate voltage is due to a surface density of positively charged donor states, $\sigma_{ss}^{+} \sim 10^{11} - 10^{12}$ cm^{-2}, which is an input parameter that is allowed to vary with temperature.

The Schrödinger equation is solved over a nanowire cross-section assumed to be lying in the xy plane. The transverse confinement results from potential barriers at surface of height equal to the electron affinity in InAs, $E_a = 4.9$ eV. The charge distribution $n(x, y)$ is calculated from the solution of 2-D Schrödinger equation as below

$$n(x,y) = \sum_i |\psi_i(x,y)|^2 \int_0^\infty f(E - E_i) g(E - E_i) dE \tag{2.3}$$

where, $g(E - E_i) = \frac{1}{\pi\hbar}\sqrt{\frac{2m^*}{(E-E_i)}}$ is the 1-D density of states per unit length, $f(E - E_i)$ is the Fermi-Dirac distribution, E_i and $\psi_i(x, y)$ are the energy and wavefunction of the i^{th} eigenstate, respectively. The above summation reduces to

$$n(x,y) = \frac{1}{\pi\hbar}\sqrt{2m^* k_B T} \sum_i |\psi_i(x,y)|^2 \times F_{-1/2}\left(\frac{E_F - E_i}{k_B T}\right) \tag{2.4}$$

where, E_F is the quasi-Fermi level and F_j is the Fermi-Dirac integral of order j and $m^* = 0.023 m_e$. The 3-D electron density n_{3D} is related linearly to $n(x, y)$ as $n_{3D}(x, y, z) = 4n(x, y)/\pi D^2$, where D is the nanowire radius. The Fermi energy E_F is determined by the net conduction electron concentration at a given gate voltage. The output charge density from the Schrödinger solver is used to calculate the next iteration of spatial potential profile using a Poisson solver. The total space charge $\rho(x, y, z)$ that goes in the Poisson equation is composed of positive and negative charge due to impurities as well as electrons and holes, given by

$$\rho(x,y,z) = e_0(N_D^+ - N_A^- - n(x,y,z) + p(x,y,z))$$

where e_0 is the single electron charge, N_D^+ is the density of ionized donors, N_A^- is the density of ionized acceptors, n and p are the electron and hole density distributions respectively. For the circular nanowire with diameter D and longitudinal axis along z axis,

$$\rho(x,y,z) = e_0(\sigma_{ss}^{+} \cdot \delta(\left|\sqrt{x^2 + y^2}\right| - D/2) - n_{3D}(x,y,z) + p(x,y,z))$$

The first term corresponds to the positive ionized donor density localized at the surface of the nanowire, n_{3D} is the electron concentration obtained from the Schrödinger solver,

the hole carrier density p is negligible for the values of donor density σ_{ss}^{+} considered here. The output of Poisson solver is fed to the Schrödinger solver to obtain the next iteration of electron charge density. The two solvers are run in sequence until the relative error in consecutive solutions of potential distribution is smaller than .1%.

Figure 2.5 shows the plot of potential at T=60 K for InAs nanowire (D = 50 nm, $L = 1\mu$m) placed on SiO_2 dielectric layer of thickness $t_{ox} = 180$ nm at a back-gate voltage of 0 V and a surface donor density of 1×10^{11} cm^{-2}. The color scale shows the potential distribution in the nanowire as well as the substrate. The inset on the right is a plot of potential profile in a cross-sectional plane of the nanowire in the middle of the FET channel, indicating the radial distribution of potential with the inset color scale. Figure 2.6 shows the calculation of first few transverse sub-bands appearing in the nanowire. The energy gap between the s-like ground state and the first excited state, $\Delta E \sim 20$ meV is quite large due to the small effective mass of electron in InAs. Electron charge distribution is calculated from the sub-bands using Fermi-Dirac integral in equation 2.4. Compared to the classical solution, in the quantum calculation, the charge distribution has a tendency to be pushed away from the surface as well as to be delocalized over the entire radial cross-section due to the large Bohr radius of electron in InAs, $a_B \sim D/2$. The charge distribution further bears a dependence on back-gate voltage and temperature conditions. At positive values of applied gate voltage the distribution is pushed towards the bottom of the nanowire and is repelled away to the top of the nanowire on application of negative gate voltages. On increasing the temperature, higher sub-bands start getting occupied as the thermal energy becomes comparable to the energy splitting between the sub-bands, $kT \sim \Delta E$.

Figure 2.7 shows comparison of the spatial distribution of carriers calculated using the Schrödinger-Poisson solver near the peak and pinch-off regimes of the conductance curve in the limits of a high and a low temperature. The panels on the left show the carrier density at the gate voltage V_{peak} corresponding to peak mobility observed experimentally at $T = 20$ K and $T = 200$ K. At 200 K, the total carrier concentration is an order of magnitude larger (due to a higher density of ionized surface states) and the charge distribution starts approaching the classical result obtained using Poisson solver with Boltzman statistics for the charge density. Note that $V_{peak} = +0.15$ V at 20 K, whereas $V_{peak} = -4.9$ V at 200 K; this is why the maximum of the charge distribution is shifted downwards (toward the backgate) at 20 K but is shifted upwards at 200 K. The panels on the right show the carrier distributions at $V_{peak} + 0.85$ V (20 K) and $V_{peak} + 1.9$ V (200 K), i.e. when the device is in the on state. An empirical study of charge proximity to surface was done as a function of temperature using the experimental values of gate voltage at peak mobility but was found to be insufficient in explaining the observed dependence of mobility.

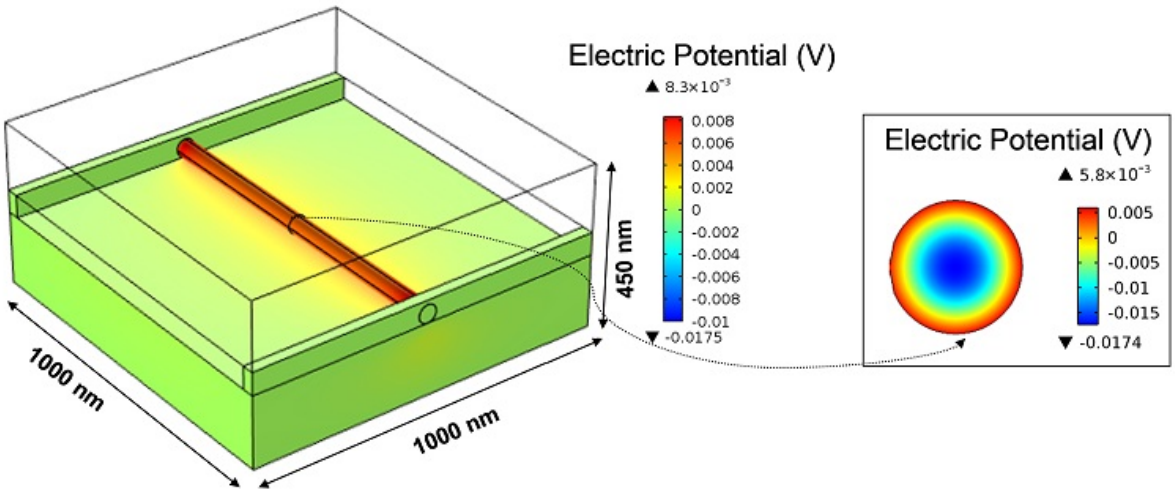

Figure 2.5: Plot of potential $V(x, y, z)$ at T=60 K for InAs nanowire of size $L = 1000$ nm, $D = 50$ nm placed on SiO_2 dielectric layer of thickness $t = 180$ nm at a back-gate voltage of $V = 0$ V and a surface donor density of $\sigma_{ss}^{+} = 1 \times 10^{11}\text{cm}^{-2}$. The two bars on either end represent the source and the drain contacts which are set to zero voltage. The inset on the right shows the potential profile along a nanowire cross-section.

2.3 Coulomb Scattering

In this section, we use the FEM model described above to calculate Coulomb impurity scattering rate from positively charged surface donor states. We chose a function $\sigma_{ss}^{+}(T) = \sigma_0 + \sigma_1 e^{-E_a/kT}$ to model the thermal activation of surface donor states as an input in the FEM model. The parameters are chosen such that the simulated electron density at zero gate voltage would roughly match the experimentally measured carrier density of device 2 at peak mobility. Note that peak mobility occurred at negative gate voltages in the real device, so the actual densities of surface donor states are likely larger than the values used in simulation. The reason for carrying out the simulations at zero gate voltage was to model the behavior for a radially symmetric wavefunction, unperturbed by the presence of a nonzero gate voltage, for simplicity. Figure 2.8(a) shows the values of $\sigma_{ss}^{+}(T)$ used in the simulations, and the resulting spatial average conduction electron density $\langle n(T) \rangle$. The parameters are $\sigma_0 = 1.7 \times 10^9\,\text{cm}^{-2}, \sigma_1 = 9.8 \times 10^{10}\,\text{cm}^{-2}$ and $E_a = 6.7$ meV for the curve in figure 2.8(a).

Mobility calculations are performed using multi-subband momentum relaxation time approximation [58]. Consider the three-dimensional eigenstates of the nanowire, $\psi(m, k) = \psi_m(x, y)e^{ikz}/\sqrt{L}$, where m is the radial subband index and k is the axial wavenumber. The transition probability $T_{k,k'}^{mn}$ between the states $|m, k\rangle$, $|n, k'\rangle$ within the 2D sub-bands m and n are calculated from Fermi's golden rule:

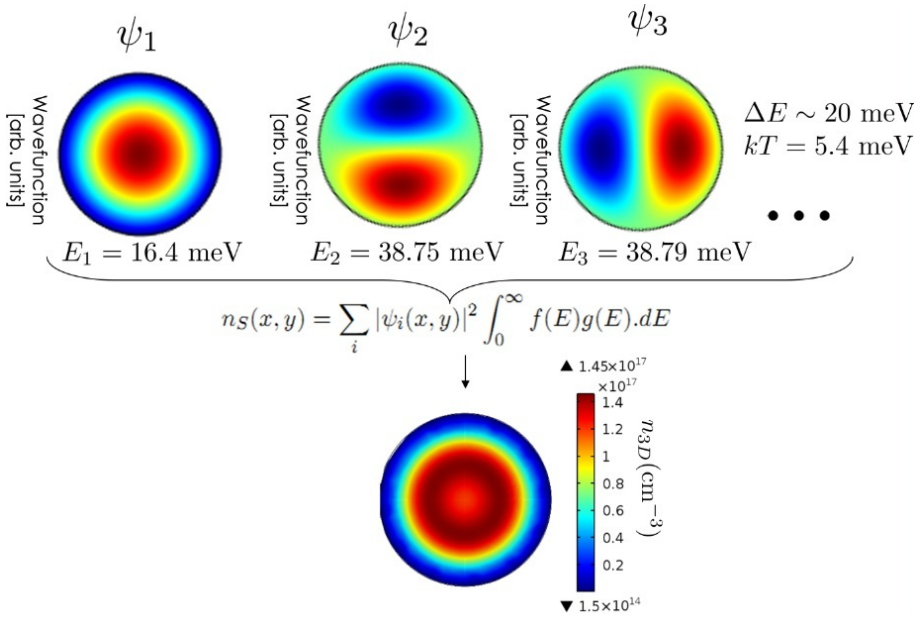

Figure 2.6: First three transverse sub-bands $\psi(x, y)$ are plotted in arbitrary units at a back-gate voltage $V = 0$ V, at surface donor density $\sigma_d = 1 \times 10^{11}\,\mathrm{cm}^{-2}$, $T = 60$ K. The maximum contribution to the spatial charge density comes from the s-like ground state. The contribution of higher orbitals is suppressed due to the relatively small magnitude of thermal energy kT at $T = 60$ K compared to the energy gap ΔE between the ground and excited states.

$$T^{mn}_{k,k'} = 2\pi/\hbar |M^{mn}_{k,k'}|^2 \delta(E_k - E_{k'}) \tag{2.5}$$

where $M^{mn}_{k,k'}$ is the scattering matrix element $\langle k, m|V_C|k', n\rangle$ resulting from the Coulomb interaction potential V_C of charged surface impurities. In our numerical simulations, V_C is obtained directly from the Poisson solver, and this takes into account the linear screening and dielectric mismatch effects [53, 59]. In the absence of these effects, V_C would be analytically expressed as a sum over unscreened point-charge potentials. In a cylindrical coordinate system (r, θ, z) where r and z are the radial and axial coordinates,

$$V_C = \sum_i V_{C,i} = \frac{e^2}{4\pi\epsilon_0\epsilon_r} \sum_i (r^2 + (D/2)^2 - rDcos\theta_i + (z - z_i)^2)^{-1/2} \tag{2.6}$$

where $V_{C,i}$ is the potential due to a single impurity located at $\boldsymbol{r}_i = (D/2, \theta, z_i)$. With the numerically-derived V_C that includes screening effects, we find that the value of $M^{mn}_{kk'}$ for a single positively charged surface impurity is on the order of 10^{-2} meV or less. Its smallness is due to the vanishing of $|\psi|^2$ at the surface, the large dielectric constant for InAs, screening effects, and that the scattering potential is attractive. In this case, treating scattering

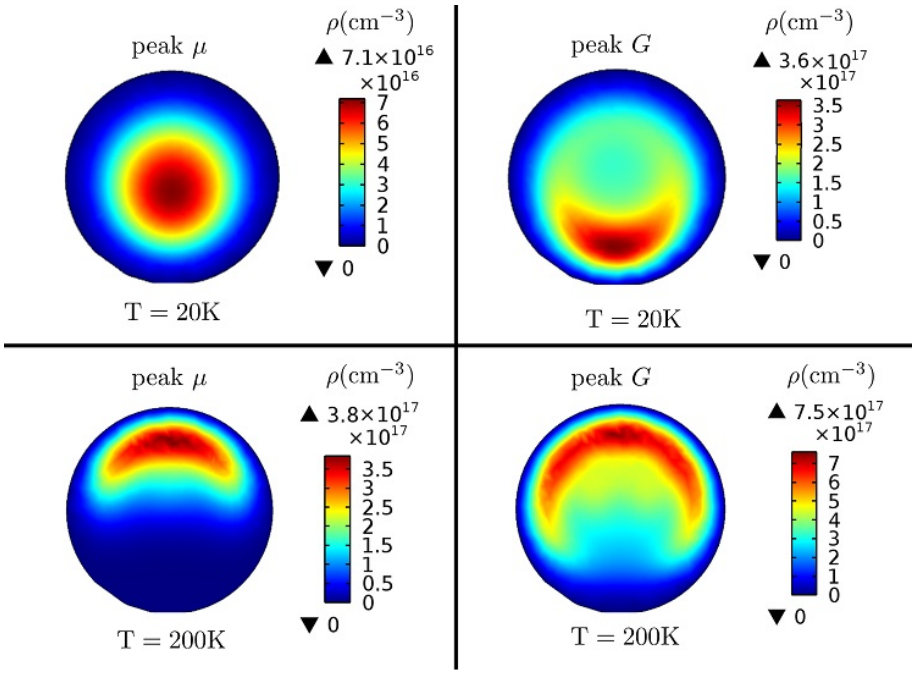

Figure 2.7: Plot showing the dependence of spatial electron charge distribution on temperature and back-gate voltage for a $D = 50$ nm nanowire, calculated by the Schrödinger-Poisson solver. The left panels show the carrier density at the gate voltage corresponding to peak mobility ($V_g = V_{peak}$) at $T = 20$ K and 200 K. Clockwise, from top left, the simulated gate voltages are $V_g = 0.15, 1.0, -3.0, -4.9$ V, respectively. At 200 K, the carrier density is much closer to the classical (Poisson only) result, since many quantum subbands are thermally occupied. At 20 K, the density is shifted considerably away from the surface, partially due to quantum confinement. The right panels shows the charge distribution at the peak conductivity in the device 'ON' state.

from single impurities independently and incoherently adding their rates can only lead to the observed mobilities if the surface impurity charge densities are unreasonably high, $N \sim 10^{13}\,\mathrm{cm}^{-2}$. At such densities, the mean separation between scatterers is too small for the picture of uncorrelated scattering to be valid. On the other hand, for a V_C that is the collective potential corresponding to a random distribution of many scatterers over the length of the nanowire, we are able to obtain the observed mobilities at impurity densities $N(T) \sim \sigma_{ss}^{+}(T)$ (see Figure 2.9). The scattering matrix element M^{mn} now roughly scales with N, rather than being independent of N in the picture of uncorrelated single-defect scattering.

The scattering matrix element is given by

$$M_{k,k'}^{mn} = \int_0^{D/2} \int_0^{2\pi} \int_{-L/2}^{L/2} r\psi_m(r,\theta) V_C \psi_n^*(r,\theta) e^{-i(k-k')z} z d\theta dr \tag{2.7}$$

where V_C is the total potential corresponding to a set of impurities. The integral in equation 2.7 has no straightforward analytical solution, so is generally solved numerically [55]. The geometry for simulating correlated scattering is indicated schematically in figure 2.9(a), and the Poisson solution V_C obtained for a random impurity distribution is shown in figure 2.9(b). The relaxation rate in subband m due to scattering into subband n is calculated as

$$1/\tau^{mn}(k) = \sum_{k'} (1 - cos\phi) T_{k,k'}^{mn} \tag{2.8}$$

where ϕ is the angle of deflection between the incoming wave vector k and the outgoing wave vector k'. The possible values of k' are given by energy conservation, $E_m + \hbar^2 k^2/2m = E_n + \hbar^2 k'^2/2m = E_F$. In 1-D geometry, only back-scattering events contribute to electron relaxation rates. When the electron concentration permits the occupation of multiple sub-bands, the relaxation rate in the m^{th} sub-band, τ_m is obtained as $1/\tau_m(k) = \sum_n 1/\tau^{mn}(k)$ where k is the initial momentum. At low temperatures or carrier densities, it is valid to only consider the relaxation time for an electron with Fermi wavenumber k_F. Making this approximation, we substitute the Fermi wavenumber in each subband k. The average relaxation time is given by $\tau(E_F) = \sum_i \tau_i n_i / \sum_i n_i$, where n_i is the population of ith subband leading to an average electron mobility $\mu = e\tau/m^*$. Figure 2.8(b) shows the Fermi wavenumbers of the first few radial subbands calculated from the Schrödinger-Poisson solutions for input donor densities $\sigma_{ss}^+(T)$. The first excited subband appears near 40 K, producing a dip in the average wavenumber $\langle k_F \rangle$. The sharp drop in Fermi velocity as temperature is lowered below 40 K strongly increases the ionized impurity scattering rate, which causes a drop in mobility.

2.3.1 Results

We performed the scattering calculations in two ways: (i) calculating integrals $M_{k,k'}^{mn}$ for the electron wavefunction and scattering potential over the entire length of the $L = 1\mu$m nanowire, and (ii) restricting the problem to a subsection of the nanowire of length $l < L$. Method (ii) is motivated by the fact that the experimentally observed mobilities suggest a mean free path $l_{mf} \sim 100 - 200$ nm, so that on average, we expect an electron traversing the nanowire to experience several uncorrelated scattering events. In the latter picture, the scattering rate τ^{-1} is calculated from the $T_{k,k'}^{mn}$ for the electron wavefunction restricted to a length l comparable to the mean free path, and the scattering rate for the entire length of nanowire is L/l times this rate. On the other hand, the probability for the electron to be in any one subsection is l/L, so these factors cancel. The only difference between the two

cases is that the 1D density of states gl, which appears in the evaluation of equation 2.8, is proportional to the subsection length. Hence, for an electron treated quantum mechanically on a length scale l (but classically on larger length scales), the density of states to scatter into is lower than if the wavefunction were spread across length L, increasing the calculated mobility. Therefore a factor L/l larger density of scatterers is required in calculation (ii) relative to (i) in order to produce the same calculated mobility.

The results of these calculations are shown in figure 2.9: (d) shows the density of scatterers N obtained by calculations (i) and (ii) that reproduce the experimental mobilities. In calculation (ii), a variable subsection length l was chosen such that $N(T) \sim \sigma_{ss}^{+}(T)$; these l values are plotted on the right axis. The calculated mobilities from (ii) are shown in figure 2.9(c) in comparison with the experimental values. A three-fold increase of N over the range 40-150 K is able to explain the observed decrease in mobility with temperature for both calculation methods. Furthermore, the density of scatterers is nearly a perfect match to the assumed ionized surface donor density for method (ii). It is reasonable to expect that the increase of N with temperature results from the thermally activated ionization of surface donor states. Confinement also plays a role in this temperature dependence, since higher radial subbands contribute to a larger electron concentration near the surface, with a corresponding increased scattering rate. However, for a fixed N, this confinement effect is too small to cause a negative slope of the mobility-versus-temperature. We find that interband scattering plays a very limited role, giving at most a correction of order 10% to the scattering rates. As expected, the positive slope of mobility below 40 K follows the behavior of the average Fermi velocity (figure 2.8(b)) over the same temperature range, where only the lowest radial subband is occupied. Overall, the simulation results confirm that scattering from charged surface states at expected densities can explain the magnitude and temperature dependence of the experimental mobilities.

2.4 Conclusions

In conclusion, we have shown evidence to support the hypothesis that ionized impurity scattering by charged surface states dominates the electron mobility in InAs nanowires across a wide range of temperatures. Transport measurements show a ubiquitous turnover in the temperature-dependent mobility at low temperatures. The decrease in mobility with temperature observed above ~ 50 K can be explained by a thermally activated increase in the number of scatterers. These results for pure InAs nanowires provide a benchmark to compare with the transport behavior of nanowires passivated by chemical means or by an epitaxial shell. Relevant to the discussion of scattering presented here is the experimentally observed correlation of stacking faults and reduced electron mobility included in Appendix A.1. It is possible that the longer zincblende sections of the nanowire may contain bound states that trap electrons [60], leading to Coulomb scattering. Gap states that trap charges locally can arise at dislocations [61], however, there are no mechanisms within the VLS

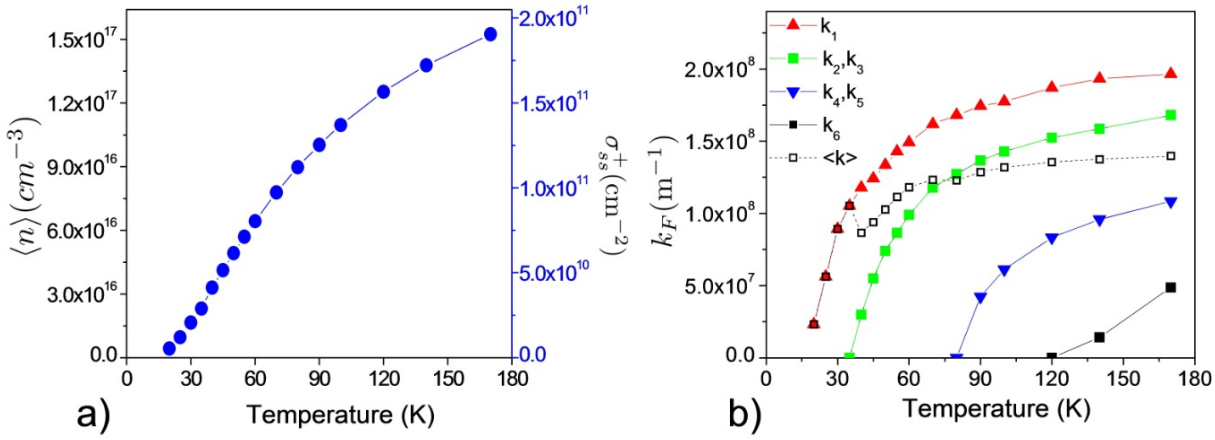

Figure 2.8: (a) The values of surface donor density, $\sigma_{ss}^{+}(T)$, used as inputs for the numerical simulation of a 50 nm diameter nanowire are shown on the right vertical axis. The functional form, described in the text, models a simple thermal activation of donors. The resulting average conduction electron densities, $\langle n(T) \rangle$, are shown on the left axis. The $\sigma_{ss}^{+}(T)$ values were chosen to produce $\langle n(T) \rangle$ at $V_g = 0$ similar in magnitude to the values observed experimentally for device 2 at peak mobility. (b) Fermi wavenumbers $k_1, ..., k_6$ of the first six radial subbands calculated from the Schrödinger-Poisson solutions for inputs $\sigma_{ss}^{+}(T)$. $\langle k \rangle$ is the average value over thermal occupation, and is proportional to the average electron velocity.

growth method through which dislocations could form for the bare (111) oriented InAs nanowires studied here.

The modelling framework developed here is extensible to the study of magneto-conductance in nanowires to further characterize their electrical and spin transport properties. In future work, it is suggested to perform calculations of mobility using a Landauer model of transport as transmission through localized impurity potential barriers which removes the perturbative approximation inherent in the use of Fermi's golden rule. A more challenging task will be to model the dynamical behavior of negatively charged trap centers found in the nanowire oxide and to study its impact on transport. The effect of negatively charged static impurities at the nanowire surface has recently been studied theoretically [62] and found to have a drastic effect on channel mobility. This is due to a strong reflection probability of an electron from a negative barrier. Such negatively charged surface states can arise in InAs nanowires in the form of charge traps present in the surface oxide. However, we do not see an evidence of charge traps limiting the mobility in our devices. The pinchoff threshold voltage shifts to more positive values as temperature is reduced, but more positive gate voltages should lead to higher occupation of negative traps. Furthermore, if oxide charge traps limited mobility, then we would expect much higher mobilities in core-shell nanowires where the oxide surface is 10-20 nm away from the core. Somewhat higher mobilities were observed in those nanowires [33], but only by a factor ∼1.4.

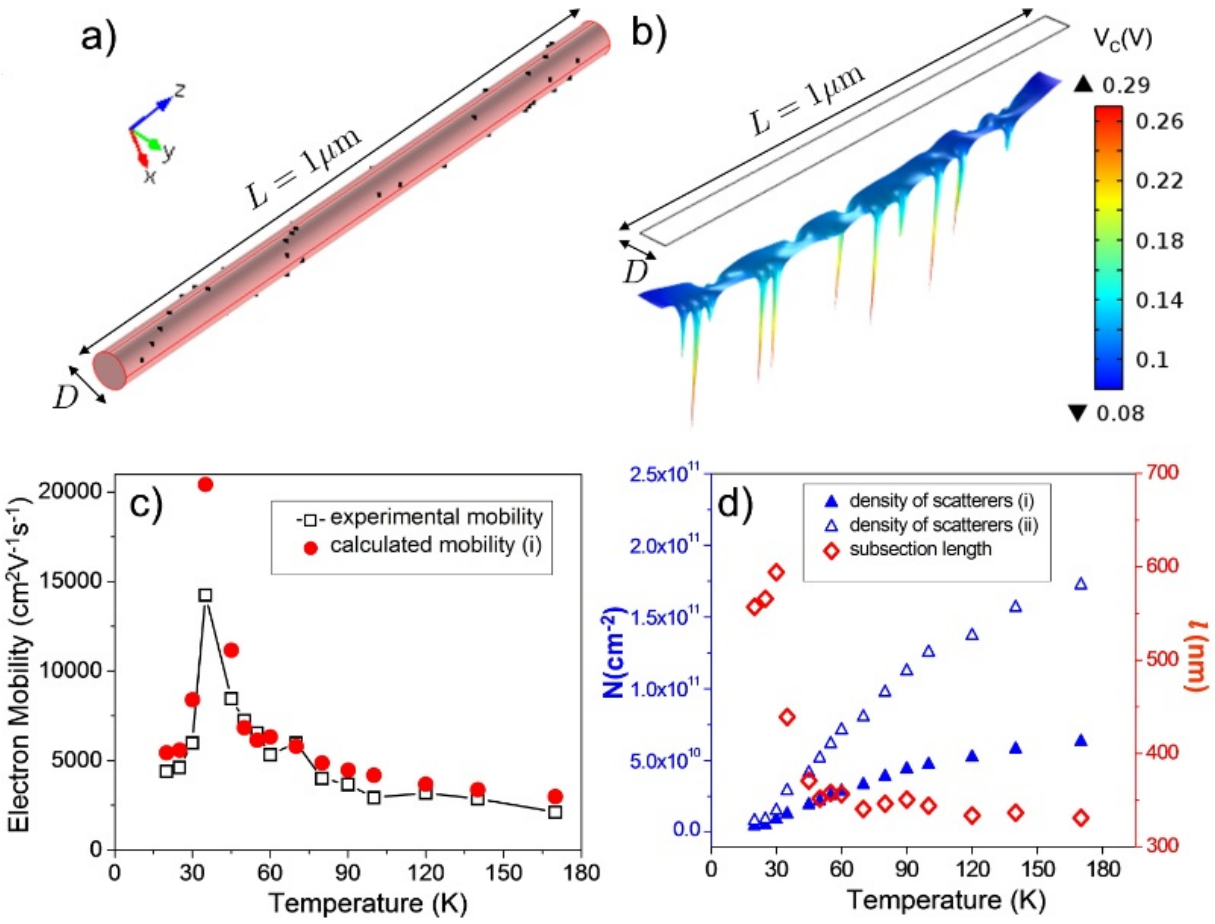

Figure 2.9: (a) Geometry used for calculating scattering from a random distribution of surface charges for a nanowire of total length L = 1 μm and diameter D =50 nm. The total scattering rate is obtained by calculating the scattering matrix elements over the entire nanowire in method (i), or by calculating the matrix elements over a subsection of length l and incoherently adding the rates from all $L = l$ sections in method (ii). (b) Poisson potential V_C corresponding to the surface charge distribution in (a), projected onto a plane along the axis of the nanowire. (c) Comparison of the experimental mobilities (device 2) and the mobilities calculated using method (i) (the results using method (ii) are nearly identical). (d) The densities of surface charges N(T) that produce the calculated mobilities in (c) for both methods. The subsection lengths l used in method (ii), loosely identified with mean free path, are shown on the right axis.

Chapter 3

Spin-Orbit Coupling and Anisotropic Exchange

A double quantum dot realized in an InAs nanowire forms a testbed system for QIP in which both single-qubit and entangling two-qubit gates can be realized, the former using SO mediated EDSR, the latter using modulation of the exchange coupling. These two mechanisms, both controlled electrically by the same local gates used to form the double dot, form a universal set of quantum gates. In the absence of the SO coupling, the interaction between a pair of electrons localized in separate quantum wells assumes a simple Heisenberg form, $H_{ex} = -J\boldsymbol{\sigma}_1.\boldsymbol{\sigma}_2$, where J is the controllable strength of exchange coupling, $\boldsymbol{\sigma}_i$ is the vector of Pauli matrices for the i^{th} spin. The form of this interaction is guided by the fact that the electronic spin and spatial degrees of freedom decouple and the requirement that the two electron wavefunction is anti-symmetric with respect to particle exchange. A strong SO coupling is needed to achieve fast single-qubit rotations through EDSR. Hence, the effect of SO interaction on the exchange coupling cannot be neglected when designing quantum gates. The SO interaction leads to additional *anisotropic* terms in the exchange Hamiltonian. It is useful in designing experiments to characterize these terms and their dependence on applied fields and gate voltages in simulations that use realistic device geometries and parameters.

In this chapter we develop numerical methods for extracting the 4×4 effective spin exchange Hamiltonian H_{spin} for a realistic nanowire double quantum dot geometry in the presence of spin-orbit coupling. The double dot is modelled by a nanowire sitting atop five narrow electrical gates in a dielectric (SiN) layer above a $SiO_2/n^{++}Si$ substrate (the doped Si substrate can be used as a global gate). We choose parameters suitable for modelling InAs nanowires. A three-dimensional electric potential inside the nanowire is obtained by an iterative Poisson-Schrödinger solver, and then projected to a one-dimensional potential along the nanowire axis for modelling exchange. The numerically exact dynamics of the full (spin and orbital) model is simulated by solving the time-dependent Schrödinger equation as a reference to compare with the dynamics calculated from the effective spin Hamiltonian. The effective spin Hamiltonian is numerically derived from the solution

of time-independent Schrödinger equation, using several methods: effective interaction method, first-order Schrieffer-Wolff method, parametric fitting of eigenvalues, truncation to the ground subspace, and a generalized numerical Heitler-London method. The first order Schrieffer-Wolff method and the truncation method were previously employed in [30] to calculate effective spin Hamiltonian for GaAs quantum dots. We find that the H_{spin} calculated using the effective interaction method produces dynamics in very good agreement with the numerically exact results in the complete Hilbert space, even in the presence of a SO coupling sufficiently strong to cause energy shifts $\Delta E_{SO} \sim 100\mu$eV.

The spin-orbit coupling is a relativistic effect incorporated as a correction in the Schrödinger equation by a Hamiltonian

$$H_{SO} = \frac{\hbar}{4m^2c^2}\boldsymbol{\sigma}.(\boldsymbol{p} \times \nabla V), \tag{3.1}$$

where ∇V is the spatial electric field experienced by an electron moving with momentum $\boldsymbol{p}$. The presence of large Dirac gap, $2mc^2 \approx 1MeV$ in the denominator suppresses this interaction for a free electron in vacuum. The magnitude of the interaction is, however, enhanced in a confined semiconductor structure due to 1) fast electron motion in strong nuclear electric fields, 2) lower symmetry of microstructures than that of vacuum [63]. The lack of spatial inversion symmetry in the crystal described as $\epsilon_\uparrow(k) \neq \epsilon_\uparrow(-k)$, when combined with the condition of time-reversal symmetry $\epsilon_\uparrow(k) = \epsilon_\downarrow(-k)$ gives rise to spin split subbands, $\epsilon_\uparrow(k) \neq \epsilon_\downarrow(k)$ even in the absence of magnetic field [64]. Here, $\epsilon_{\uparrow(\downarrow)}(k)$ is the energy of spin-up(down) subband at momentum k. We consider InAs nanowires that exhibit a wurtzite [65] crystal structure as seen in the study of electron transport in Chapter two. The form of spin-orbit coupling in such nanowires is dictated by the symmetries of the wurtzite crystal (bulk inversion asymmetry) and the nanowire confinement (structure inversion asymmetry). The former contribution stems directly from the bulk conduction band spin-splitting in materials that lack inversion symmetry of the crystal lattice called the Dresselhaus [14] component while the second contribution arising from the asymmetry of confining potential is called the Rashba component [16]. We consider the 1-D limit where the strongest confinement is provided by the nanowire walls. If cubic-in-momentum terms are neglected , the general form for the SO interaction for the case of axial confinement is [64]

$$H_{SO} = (\boldsymbol{p}.\boldsymbol{c})(\boldsymbol{\eta}.\boldsymbol{\sigma}), \tag{3.2}$$

where $\boldsymbol{p}$ is the (kinetic) momentum vector, $\boldsymbol{c}$ is a unit vector along the [0001] crystallographic direction, $\boldsymbol{\eta}$ gives the direction and magnitude of the spin-orbit field, and $\boldsymbol{\sigma} = (\sigma_x, \sigma_y, \sigma_z)$ is the vector of Pauli matrices. The effects of structure inversion asymmetries (SIA) and bulk inversion asymmetries (BIA) are included in Eq. (3.2), resulting in an arbitrary linear combination of Rashba [16] and linear-Dresselhaus [14] type interactions. The [0001] crystallographic direction of wurtzite InAs aligns with the nanowire growth axis, which we label as the $\hat{\boldsymbol{x}}$ direction, simplifying Eq. (3.2) to

$$H_{SO} = (p_x)(\boldsymbol{\eta}.\boldsymbol{\sigma}). \tag{3.3}$$

We choose Eq. (3.3) as the general form describing the SO interaction in InAs nanowires.

In the presence of SO interaction, the eigensolutions to the total Hamiltonian describing two interacting electrons are not generally spin-separable, i.e. spin is no longer a good quantum number. When the SO interaction is sufficiently weak, its effects can be gauged away [25, 30] and the double dot spin dynamics can be determined with high precision by an effective 4×4 spin Hamiltonian. The following general form is obtained for effective interaction between spins, deduced independently in [24] and in [27] from the axial symmetry of the interaction about the spin-orbit field: an isotropic exchange term proportional to J' (here J' in the general case is distinguished from the isotropic exchange strength J in the absence of SO coupling), a Dzyaloshinskii-Moriya term proportional to $\boldsymbol{\beta}$ which is first order in SO coupling, and a second order pseudo-diploar term proportional to unitless scalar γ:

$$H_{spin} = J'(\boldsymbol{\sigma}_1.\boldsymbol{\sigma}_2 + \boldsymbol{\beta}.(\boldsymbol{\sigma}_1 \times \boldsymbol{\sigma}_2) + \gamma(\boldsymbol{\beta}.\boldsymbol{\sigma}_1)(\boldsymbol{\beta}.\boldsymbol{\sigma}_2)). \tag{3.4}$$

The exchange coefficients J', $\boldsymbol{\beta}$ and γ depend on the double well potential profile, the spin-orbit fields and the external magnetic field.

Anisotropic exchange in SO coupled double quantum dots has been previously studied both as a useful tool for designing quantum gates [29] and as an error source to be mitigated [30, 69, 25]. The theory of effective spin Hamiltonian in the presence of a perturbatively weak spin-orbit coupling has been developed for a decade now but there hasn't yet been an experimental realization of two qubit gate utilizing this interaction. In this chapter we try to bridge this gap between theory and experiment. We perform an operational characterization of the spin Hamiltonian in terms of experimentally accessible control paramters that will guide the design of gates using this interaction. A numerical study is appropriate for InAs based quantum dots due to the relatively strong SO interaction which renders the accuracy of an analytical perturbative approach to be questionable.

Our method for calculating the effective spin Hamiltonian (H_{spin}) consists of two main steps. First, we iteratively solve coupled Poisson-Schrödinger equations to calculate the double well potential, optimizing the tuning by the local electrostatic gates to model a realistic two-electron case. We then construct the total Hamiltonian, H_{tot}, governing the spatial and spin components of the electrons. H_{tot} is numerically diagonalized, obtaining eigenstates that have support over both the spatial and spin eigenspaces. In step two, H_{spin} is obtained by reducing to the 4-dimensional Hilbert space of the spins, while retaining the influence of the orbital-spin eigenstates. This is achieved using an effective interaction method [72, 70, 71, 73] well known in many-body problems [74, 75, 76]. Finally, the values for the anisotropic exchange coefficients are extracted using a crystal-field approach [75]. For comparison, we report on several additional methods for estimating the reduced spin Hamiltonian, described below. We quantify the accuracy of these methods by comparing the outcome of the time evolution of selected spin states under H_{spin} with the outcome of the time evolution of the entire system under H_{tot} projected to the spin subspace.

The chapter organization is as follows: in Sec 3.1 we describe the finite element model for a gated InAs nanowire double dot. In Sec 3.2 we describe in more detail the numerical methods for obtaining the double well potential profile and solving the Schrödinger equation of the system. We then discuss several approaches for deriving H_{spin} from the numerical results. In Sec 3.3, we analyze the accuracy of H_{spin} in describing the dynamics, and present results on the parametric dependence of H_{spin} on the central barrier gate voltage and the external magnetic field. Finally, we summarize and discuss the results in Sec 3.5.

3.1 Device Model

The finite element model (Comsol Multiphysics) incorporates an InAs nanowire of diameter 50 nm and length 1 μm sitting atop a set of five local gate electrodes with center-to-center spacing of 60 nm. These gates are embedded in a 20 nm thick SiN dielectric layer above 200 nm-thick SiO_2 with a global gate electrode underneath. A schematic of the model is shown in Fig. 3.1a. The local and global gate voltages are adjusted to produce a double well potential at carrier densities consistent with few electron dots at a temperature $T = 1$ K.

We consider a uniform distribution of nanowire surface states when calculating the longitudinal potential profile inside the nanowire. We take this into account by including a positively charged surface donor density $\rho_{surf} = 1 \times 10^{11}\,\mathrm{cm}^{-2}$, a value consistent with the results of transport studies in the previous chapter. We then treat the nanowire as a quasi-1D system at low temperatures due to strong radial confinement resulting from the low electron effective mass m^* in InAs. The transverse sub-bands due to radial confinement are split by a gap of ~ 25 meV compared to the thermal energy $k_BT = 0.086$ meV at $T = 1$ K. Hence, we project the 3D double well potential to a 1D axial potential to simplify further numerical analysis. The 1-D axial potential extends over a length $L = 250$ nm. Under the assumption of quasi-1D geometry, the transverse wavefunctions are approximated by ground state harmonic oscillator solutions. The electrostatic Coulomb interaction between a pair of electrons located at coordinates (r_1, r_2) takes the following form [77].

$$H_C(r_1, r_2) = \frac{e^2\sqrt{\pi\alpha}}{4\pi\epsilon_0\epsilon_r} e^{\alpha|r_1-r_2|^2} \mathrm{erfc}(\sqrt{\alpha}|r_1 - r_2|) \tag{3.5}$$

where $\alpha = m^*\omega_\perp/(2\hbar)$, $\hbar\omega_\perp$ is the excitation energy of the electron transverse motion calculated to be ~ 20 meV for D=50 nm nanowire.

The 1D Hamiltonian of the two electron system H_{tot} is composed of an orbital term H_0, a

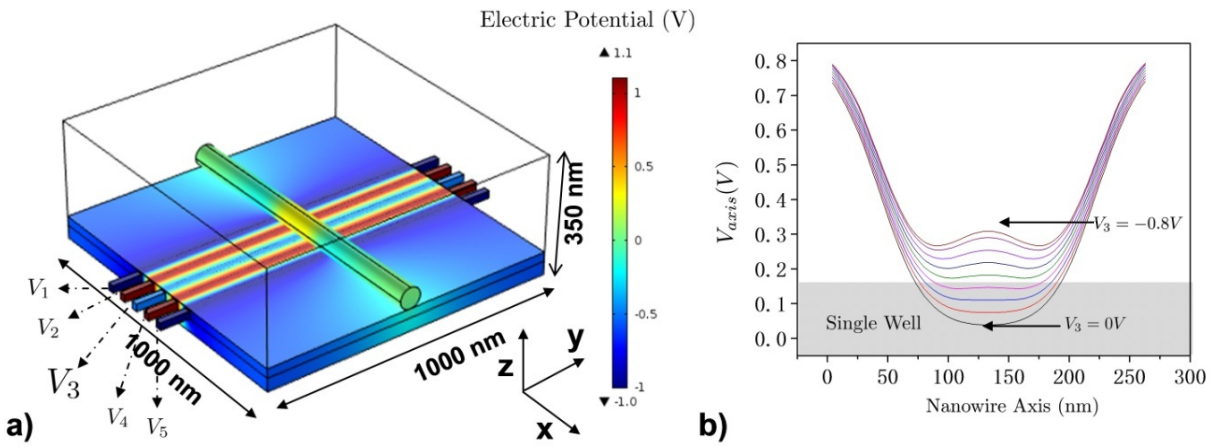

Figure 3.1: a) Geometry of the simulated nanowire device with fine local gates embedded inside a 20 nm thick SiN layer which separates the nanowire from the SiO_2 dielectric layer; exchange coupling between the dots is modulated by an externally applied voltage on the central local gate marked V_3. The voltage applied at the side and plunger gates are $V_1 = V_5 = -1.7\,\mathrm{V}$ and $V_2 = V_4 = 0.4\,\mathrm{V}$, respectively. b) 1-D projection of the potential, V_{axis} obtained from the Poisson-Schrödinger solver at $T = 1$ K along the nanowire axis for a range of values of V_3; the system enters a single well regime as V_3 approaches 0 V.

Zeeman term H_Z, a spin-orbit term H_{SO}, and the Coulomb repulsion term H_C:

$$\begin{aligned} H_{tot} &= H_0 + H_C + H_Z + H_{SO}; \\ H_0 &= (\boldsymbol{P}_1^2/2m^* + \boldsymbol{P}_2^2/2m^* + V(r_1) + V(r_2)) \otimes \mathbb{I}, \\ H_Z &= g^*\mu_B \boldsymbol{B}\cdot\sigma_1 + g^*\mu_B \boldsymbol{B}\cdot\sigma_2, \\ H_{SO} &= \boldsymbol{p}_{x_1}(\boldsymbol{\eta}\cdot\boldsymbol{\sigma}_1) + \boldsymbol{p}_{x_2}(\boldsymbol{\eta}\cdot\boldsymbol{\sigma}_2), \end{aligned} \tag{3.6}$$

where μ_B is the Bohr magneton, r_i is the position coordinate of the i^{th} electron, $V(r_i), i = 1, 2$ is the 1-D projection of the potential derived from Poisson-Schrödinger solver, ϵ_0 is the vacuum dielectric constant, and g^* is the effective electron g-factor taken to be $g^* = 8$ as calculated from the Zeeman splitting of orbitals in [17]. The kinetic momentum $\boldsymbol{P} = \boldsymbol{p} + e\boldsymbol{A}$ is expressed using the canonical momentum $\boldsymbol{p}_i = -i\hbar\boldsymbol{\nabla}_i$ and the vector potential $\boldsymbol{A}$ that satisfies $\boldsymbol{B} = \boldsymbol{\nabla}\times\boldsymbol{A}$. $\mathbb{I}$ is the identity operator acting on the spins. The Cartesian coordinate system used is depicted in Fig. 3.1a. The strengths of the Rashba and Dresselhaus interaction terms in H_{SO} are η_x and η_y, respectively (see Appendix C.4). For most calculations, we chose the SO vector $\boldsymbol{\eta}$ to lie in the $x-y$ plane at an angle of 45^o to the x-axis with a magnitude $|\boldsymbol{\eta}| = 15\,\mathrm{meV.nm}$, corresponding to equally strong Rashba and Dresselhaus couplings [69, 3]. For completeness, we also analyze cases with different orientations of the SO vector $\hat{\boldsymbol{\eta}}$ in the $x-y$ plane as well as different SO coupling strengths $|\boldsymbol{\eta}|$. Fig. 3.1b shows a set of one-dimensional double-well potential profiles obtained by

projecting the solution of self-consistent 3-D Poisson-Schrödinger solver along the nanowire axis. The local gate voltage V_3 is varied from -0.75 V to 0 V corresponding to the transition of two-electron double well system from weakly interacting regime at V_3 =-0.75 V to a single dot regime at V_3 =0 V.

3.2 Methods of constructing effective spin Hamiltonian

The two-electron double dot system Hamiltionian described above is solved numerically to obtain the spin-orbit eigenspectrum and the eigenstates, which are then used to construct an effective spin Hamiltonian in the four dimensional subspace of two electron spins. In the next section, we present the details of the Schrödinger solver followed by the methods of constructing effective spin Hamiltonian.

Step I: Numerical diagonalization of H_{tot}

In order to diagonalize H_{tot}, the Schrödinger equation $H_{tot}\chi = \epsilon_\chi \chi$ is specified as four coupled linear differential equations, in the basis of two independent position variables $r_1, r_2 \in \mathbb{R}$ and two spins. The system of equations is solved using the numerical finite element method. The eigenfunctions $\chi(r_1, r_2) \in (L_2(\mathbb{R}) \otimes \mathbb{C}^2)^{\otimes 2}$ are represented in the following spinor form:

$$\chi(r_1, r_2) = \begin{bmatrix} \phi_{S_0}(r_1, r_2) \\ \phi_{T_-}(r_1, r_2) \\ \phi_{T_0}(r_1, r_2) \\ \phi_{T_+}(r_1, r_2) \end{bmatrix}, \tag{3.7}$$

where $s \in \{S_0, T_-, T_0, T_+\}$ is the spin state of the two electrons in the singlet-triplet basis, where the subscripts $\pm$ and 0 indicate the angular momentum projections $\pm\hbar$ and 0, respectively. $\phi_s(r_1, r_2)$ are the spatial wavefunctions that are symmetric or antisymmetric depending on s . The Schrödinger equation is solved over a 2D rectangular domain of size $L \times L$ with $\sim$ 1000 mesh elements. A Dirichlet boundary condition $\phi_s = 0$ is enforced along the domain boundary. A constraint corresponding to the particle exchange symmetry or anti-symmetry, $P\phi_s(r_1, r_2) = \pm\phi_s(r_1, r_2)$, is applied to the spatial wavefunctions $\phi_s(r_1, r_2)$. Here, P is the particle exchange operator and the sign depends on the spin state s. This guarantees the antisymmetry of the total wavefunctions. Fig. 3.2 shows a plot of the eigenfunctions of the static Hamiltonian, H_{tot} at $V_3 = -0.65\,\mathrm{V}$ in the presence of Zeeman interaction, $\boldsymbol{B} = (90\,\mathrm{mT})\hat{\boldsymbol{z}}$ and spin-orbit vector given by $\boldsymbol{\eta} = \frac{15}{\sqrt{2}}(\hat{\boldsymbol{x}} + \hat{\boldsymbol{y}})\,\mathrm{meV.nm}$. The spatial wavefunction respects the particle exchange symmetry/anti-symmetry as required by the Pauli principle. This can be seen as the reflection symmetry/anti-symmetry of the plotted wavefunction with respect to the diagonal. The vanishing amplitude of the

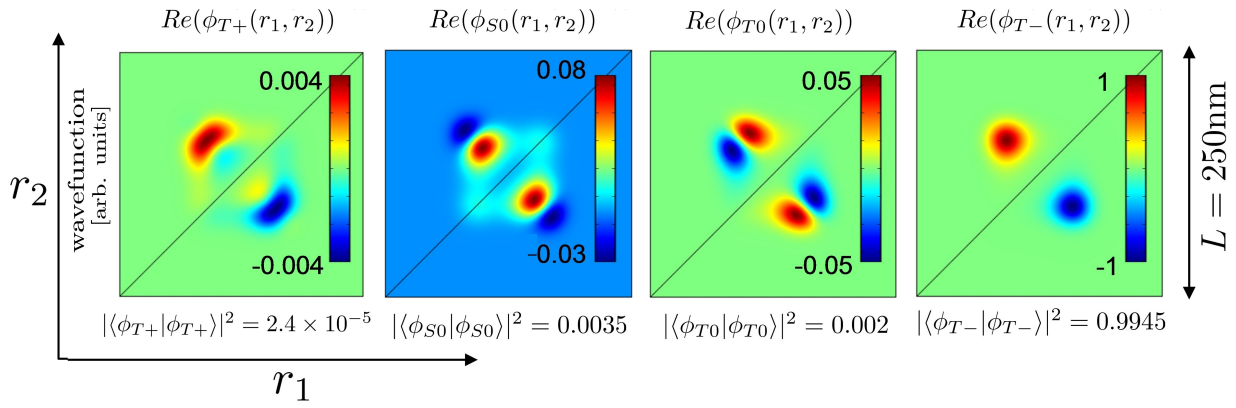

Figure 3.2: Real part of the ground state wave function $\chi_1(r_1, r_2)$ obtained from diagonalization of H_{tot}, at $V_3 = -0.65\,V$ in a magnetic field $B_z = 90$ mT, with SO interaction $|\boldsymbol{\eta}| = 15\,\text{meV.nm}$ and $\hat{\boldsymbol{\eta}} = (\hat{\boldsymbol{x}} + \hat{\boldsymbol{y}})/\sqrt{2}$. The state shows a $|T-\rangle$ like character since the Zeeman energy is larger than isotropic exchange in this case.

wavefunction at the diagonal indicates that the double dot occupancy errors are small and the electrons are localized in separate quantum dots.

Further, the time evolution of the system in the full Hilbert space is calculated numerically by solving the Schrödinger equation

$$H_{tot}\chi(r_1, r_2, t) = i\hbar\frac{\partial}{\partial t}\chi(r_1, r_2, t), \tag{3.8}$$

with time t and coordinates r_1, r_2 as independent variables. We choose an initial state $\chi(t = 0)$ that corresponds to a reduced-dimension spin state from the set $\left\{|S_0\rangle, |T_0\rangle, \frac{|S_0\rangle \pm |T_0\rangle}{\sqrt{2}}, \frac{|S_0\rangle \pm i|T_0\rangle}{\sqrt{2}}\right\}$. The details of the solver are provided in Appendix B.

Step II: Constructing 4×4 spin Hamiltonian

A standard approach to construct an effective Hamiltonian that acts on a low-energy subspace of the full Hilbert space $\mathfrak{H}$ of a Hamiltonian H_{tot} is to apply a Schrieffer-Wolff transformation [78] to H_{tot} so as to decouple, up to a desired order of perturbation theory, the low-energy subspace form the rest of $\mathfrak{H}$. However, this method gives an effective Hamiltonian in a rotated basis that is no longer spin separable (c.f. sec 3.2.2). However, for the purposes of this study we want to restrict ourselves to a separable spin basis of pure singlets and triplets.

Here we employ a slightly unusual approach of 'effective interaction theory' [71, 75] to construct a spin Hamiltonian H_{spin}, represented in the basis of Eq (3.7), acting on the low

energy subspace of the numerically diagonalized H_{tot}. The unknown coefficients $\{J', \boldsymbol{\beta}, \gamma\}$ appearing in Eq (3.4) are derived from H_{spin} using a crystal-field approach [75]. The results are compared with alternative methods of calculating these coefficients as described in the next sections.

3.2.1 Method A. Effective Interaction Theory

Theories of effective interaction [72, 70, 71, 73] have been used in many-body physics problems ranging from quantum chemistry to nuclear physics [74, 75, 76]. In this approach, a full Hilbert space Hamiltonian H is transformed into an effective Hamiltonian h_m that acts on a restricted subspace, called the model space, of dimension m. According to Bloch's [79] and des Cloizeaux's theory [80], it is possible to define h_m such that the m eigenvalues match exactly those of the exact Hamiltonian and the m eigenfunctions are the projections of the exact wave functions onto the model space. The effective Hamiltonian h_m can be viewed as an operator acting in the model space that incorporates information about the original interactions in the complete space of H.

The numerical calculation of the restricted space Hamiltonian h_m relies on the eigenvalues and the projection of eigenvectors of the full Hamiltonian H on the model space. We choose a basis set for the model space in our problem as

$$\{\xi_j\}_{j=1-4} = \{\psi_S S_0, \psi_{AS} T_-, \psi_{AS} T_0, \psi_{AS} T_+\}, \tag{3.9}$$

where $\psi_{S(AS)}$ is the lowest symmetric (anti-symmetric) spatial wavefunction of the SO free Hamiltonian $(H_{tot} - H_{SO})$. The SO eigenvectors $\chi_i, i = \{1, 2.., m\}$ of H_{tot}, are projected onto this model space as

$$\Psi_i = \sum_{j=1}^{4} |\xi_j\rangle V_{ji}, \tag{3.10}$$

where $V_{ji} = \langle \xi_j | \chi_i \rangle, (i, j = 1, .., 4)$, is the projection of first $m = 4$ eigenstates onto the model space. This leads to a spectral definition of the effective spin Hamiltonian as

$$h_m = \sum_{i=1}^{m} E_i |\Psi_i\rangle\langle\Psi_i| = V E V^{-1}, \tag{3.11}$$

where E is a diagonal matrix of eigenvalues, $E = \{E_1, E_2, E_3, E_4\}$. However, this construction is not guaranteed to yield a Hermitian matrix as the eigenvectors defining the columns of V are neither orthogonal nor normalized. The projections are orthogonalized by a $S^{-1/2}$ transformation proposed by [80] given by $V_K = (VV^\dagger)^{-1/2} V$. Here S is the overlap matrix of the projected wavefunctions. This allows the definition of a Hermitian effective Hamiltonian

$$H_{spin} = V_K E V_K^{-1}. \tag{3.12}$$

Finally, the extraction of anisotropic coefficients $\{J', \boldsymbol{\beta}, \gamma\}$ from the numerical Hamiltonian H_{spin} is done using the crystal-field approach as follows. An effective Hamiltonian described by n parameters may be written in terms of a complete set of operators as

$$H_{spin} = \sum_{i=1}^{n} X_i T_i, \tag{3.13}$$

where T_i are the spin operators in Eq (3.4) corresponding to the interactions in the model space, including the Zeeman interaction with an external field. $X_i, i = \{1, \ldots, n\}$, are the n unknown coefficients in the Hamiltonian. Following [75], the parameters X_i are calculated as

$$X_i = \sum_{j=1}^{n} (A^{-1})_{ij} \mathrm{tr}(T_j^{\dagger} H_{spin}), \tag{3.14}$$

where $A_{ij} = \mathrm{tr}(T_j^{\dagger} T_i)$, since the operators $T_i, i \in \{1, \ldots, n\}$, are linearly independent. In principle, H_{spin} constructed this way is as precise as the full Hamiltonian in the sense of predicting exact eigenvalues, as long as all the interactions are taken into account in the general form of H_{spin} (Eq (3.4)). A rigorous analysis of the convergence properties of the effective interaction method is not available, however, they have enjoyed great success in the nuclear physics community.

3.2.2 Method B: Degenerate Perturbation Theory

Here, we look at an approach based on formalized version of degenerate perturbation theory known as Schrieffer-Wolff transformation. The main idea is to apply a unitary $U = e^S$ to the exact Hamiltonian H_{exact} that decouples the low energy subspace from the rest of the Hilbert space.

$$e^S H_{exact} e^{-S} = \begin{pmatrix} H_{low} & 0 \\ 0 & H_{high} \end{pmatrix} \tag{3.15}$$

A unitary to this effect is introduced in [30] to extract an effective spin Hamiltonian in the presence of SO interaction. The first order SO term in H_{tot} is gauged away by performing a Schrieffer-Wolff transformation, $\tilde{H} = e^S H_{tot} e^{-S}$, where

$$S = -\frac{i}{2}(x_1 \boldsymbol{n}_1.\boldsymbol{\sigma}_1 + x_2 \boldsymbol{n}_2.\boldsymbol{\sigma}_2) \tag{3.16}$$

The vectors $\boldsymbol{n}_i$ depend on SO coupling, $\boldsymbol{n}_i = (1/l_D, 1/l_R, 0)$ where $l_D = \hbar^2/2m^*|\boldsymbol{\eta}_x|$, $l_R = \hbar^2/2m^*|\boldsymbol{\eta}_y|$ are the effective spin-orbit lengths corresponding to Dresselhaus and Rashba contributions, respectively. In the absence of an external magnetic field, $\tilde{H}$ reduces to an isotropic spin Hamiltonian up to a SO induced constant energy shift. It is noted that the transformed Hamiltonian $\tilde{H}$ acts on a unitarily transformed basis of spins $U|\xi_j\rangle_{j=\{1-4\}}$. The rotation of $\tilde{H}$ can be undone approximately by replacing the spatial coordinate x with

its mean value $\langle x \rangle = \pm a$, so that $U_a = e^{-i\frac{a}{2}(\boldsymbol{n}_1.\boldsymbol{\sigma}_1 - \boldsymbol{n}_2.\boldsymbol{\sigma}_2)}$. Applying U_a gives an approximate effective spin Hamiltonian in the original unrotated basis . We calculate $\{J', \boldsymbol{\beta}, \gamma\}$ from the numerically obtained Hamiltonian $U_a^\dagger \tilde{H} U_a$. This method only requires the numerical solution of SO free Hamiltonian, $H_{tot} - H_{SO}$. The information about the exchange strength J and the dot separation a is sufficient to implement the approximate unitary transform giving H_{spin} in the singlet-triplet basis.

3.2.3 Method C: Parametric Fitting of the Energy Eigenvalues

In this method, we make a direct correspondence between the energy eigenvalues of the exchange Hamiltonian, Eq. (3.4) and the numerically calculated eigenspectrum of H_{tot}. The solution of algebraic equations obtained by equating the two sets of eigenvalues yields the unknown parameters in Eq.3.4. This method is constrained in terms of the number of free parameters that can be extracted, only providing $\{J', |\boldsymbol{\beta}|, \gamma\}$, and gives valid solutions over a restricted range of conditions. In particular, when no external magnetic field is present, the eigenvalues of the effective spin Hamiltonian in Eq. (3.4) are two-fold degenerate, given by

$$\{\lambda\} = \begin{Bmatrix} -J' - 2J'\sqrt{1+|\boldsymbol{\beta}|^2} - J'\gamma|\boldsymbol{\beta}|^2 \\ J' + J'\gamma|\boldsymbol{\beta}|^2 \\ -J' + 2J'\sqrt{1+|\boldsymbol{\beta}|^2} + J'\gamma|\boldsymbol{\beta}|^2 \\ J' + J'\gamma|\boldsymbol{\beta}|^2 \end{Bmatrix}, \tag{3.17}$$

These are compared with the numerically calculated energy level splittings of the lowest SO states χ_j to extract the unknowns $J', |\boldsymbol{\beta}|, \gamma$. In order to deal with the degeneracy at $\boldsymbol{B} = 0$, an additional condition is required in the calculation of unknown coefficients (see Appendix C.1). On adding a Zeeman term, the method is seen to have an artificial dependence on the magnitude of the external magnetic field; when Zeeman splitting exceeds the exchange splitting, $g^*\mu_B B > J'$ imaginary solutions are obtained for the coefficient $|\boldsymbol{\beta}|$ which are physically disallowed. The knowledge of numerical eigenfunctions is not utilised in this method.

3.2.4 Method D: Truncation

Consider the basis $\{\xi_j\}$ given in Eq. (3.9). By restricting H_{tot} to this basis, an effective 4×4 spin Hamiltonian H_{spin} corresponding to H_{tot} is constructed by simple truncation as

$$(H_{spin})_{ij} = \langle \xi_i | H_{tot} | \xi_j \rangle = (J\boldsymbol{\sigma}_1.\boldsymbol{\sigma}_2)_{ij} + \langle \xi_i | H_{SO} | \xi_j \rangle, \tag{3.18}$$

where $\{i, j = 1, \ldots, 4\}$. Using the spin-orbit selection rules [30], the second term above can be written in terms of spin operators as

$$\langle \xi_i | H_{SO} | \xi_j \rangle = \boldsymbol{\beta}_1 \cdot (\boldsymbol{\sigma}_1 \times \boldsymbol{\sigma}_2) + \boldsymbol{\beta}_2 \cdot (\boldsymbol{\sigma}_1 - \boldsymbol{\sigma}_2), \tag{3.19}$$

where $\boldsymbol{\beta}_1$ and $\boldsymbol{\beta}_2$ are proportional to the strength of SO interaction:

$$\boldsymbol{\beta}_1 = \mathrm{Im}\langle\psi_S|(\boldsymbol{p}_{x_1} - \boldsymbol{p}_{x_2}) \cdot \boldsymbol{\eta}|\psi_{AS}\rangle, \quad \boldsymbol{\beta}_2 = \mathrm{Re}\langle\psi_S|(\boldsymbol{p}_{x_1} - \boldsymbol{p}_{x_2}) \cdot \boldsymbol{\eta}|\psi_{AS}\rangle. \tag{3.20}$$

We thus obtain

$$H_{spin} = J(\boldsymbol{\sigma}_1.\boldsymbol{\sigma}_2) + \boldsymbol{\beta}_1.(\boldsymbol{\sigma}_1 \times \boldsymbol{\sigma}_2) + \boldsymbol{\beta}_2.(\boldsymbol{\sigma}_1 - \boldsymbol{\sigma}_2). \tag{3.21}$$

Note that J here is not modified by the SO coupling, but rather corresponds to case $\boldsymbol{\eta} = 0$. The parameters $\boldsymbol{\beta}_1, \boldsymbol{\beta}_2$ are directly related to the coefficient vector $\boldsymbol{\beta}$ in Eq. (3.4). The relative strength of $\boldsymbol{\beta}_1, \boldsymbol{\beta}_2$ is subject to an arbitrary choice of the relative phase of the wavefunctions ξ_i, and the observable quantity is $|\boldsymbol{\beta}| = \sqrt{|\boldsymbol{\beta}_1|^2 + |\boldsymbol{\beta}_2|^2}$. This method is clearly disadvantageous because it does not capture the modification of J by the SO coupling, nor does it capture γ.

3.3 Results

In this section, we present a comparison of the effective spin Hamiltonians H_{spin} constructed using methods A-D described above, and use them to study spin dynamics in the 4×4 Hilbert space when exchange is pulsed on. A state fidelity measure is used to compare the final states obtained via evolution under H_{spin} to those obtained by solving the time dependent Schrödinger equation in the full Hilbert space and projecting the final state to the low energy subspace. We also calculate the dependence of $\{J', \boldsymbol{\beta}, \gamma\}$ on the central barrier gate voltage V_3, the external magnetic field $\boldsymbol{B}$, and the SO coupling $\boldsymbol{\eta}$.

3.3.1 Gate voltage dependence

In order to proceed with characterizing the dependence of effective spin Hamiltonian on experimentally accessible parameters, we begin with studying the modulation of exchange through the handle of voltage control of central barrier. Fig. 3.3a shows the isotropic exchange parameter J and the interdot separation $2a$, calculated using the numerical finite element method. Here, there is no external magnetic field or SO coupling, $\boldsymbol{B} = 0$, $\boldsymbol{\eta} = 0$. We observe an exponential decrease in J from 2×10^{-3} eV at V_3 =0 V to $J = 2 \times 10^{-8}$ eV at V_3 =-0.75 V. High values of exchange interaction results in InAs due to its large Bohr radius, allowing for stronger overlap of the single-dot electron wavefunctions, $a_B = \epsilon \frac{m_e}{m*} a_0$, where a_0 is the Bohr radius in vacuum. For the purposes of QIP, it is detrimental to operate in a double dot regime resembling a single quantum well as an unbounded increase in J would eventually result in excitations out of the designated subspace of two qubits. This sets an upper bound on the strength of J in a practical gate design. The lower bound is set by the requirement of achieving fast coupled gates such that the decoherence errors accumulated during the gate operation lie below the threshold for fault tolerant quantum computation. Referring back to fig. 3.3a, the dot separation $2a$ is seen to respond almost

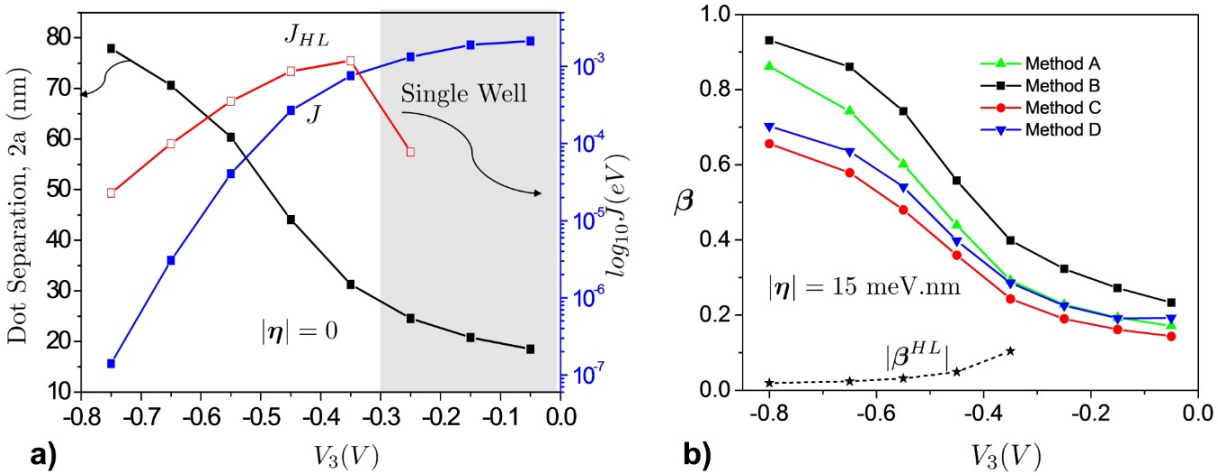

Figure 3.3: a) Plot of interdot separation $2a$ and isotropic exchange energy J in the absence of SO interaction and external magnetic field, calculated using the numerical finite element method (blue) and the generalized Heitler-London method (red) as a function of barrier gate voltage V_3. We observe that J decreases exponentially with barrier gate voltage in the well-separated regime, but the rate of the response slows in the single well regime. The dot separation increases almost linearly by ~ 50 nm over this range of gate voltages, demonstrating the electrostatic tunability of the FEM model. b) The first-order anisotropic parameter $|\boldsymbol{\beta}|$ calculated as a function of barrier voltage V_3 in the presence of a large SO coupling, $\boldsymbol{\eta} = (15 \text{ meV.nm})(\hat{\boldsymbol{x}} + \hat{\boldsymbol{y}})/\sqrt{2}$ and zero external magnetic field, using methods A-E described in the text. Methods A-D yield $|\boldsymbol{\beta}|$ that increases monotonically with the barrier height, explained by the increase in the electric dipole moment of the two electrons as they are separated. The Heitler-London method fails to capture the correct qualitative behavior of $|\boldsymbol{\beta}|$.

linearly to the barrier height, and can be varied over a range of ~ 50 nm by varying V_3 from -0.05 V to -0.75 V. Fig. 3.3b presents a comparison of the first-order anisotropic parameter $|\boldsymbol{\beta}|$ calculated using methods A-D in zero external magnetic field. The different methods give qualitatively similar results in which $|\boldsymbol{\beta}|$ increases monotonically with $|V_3|$. Larger anisotropy at larger separation can be explained by the increase of the electric dipole moment of the two-electron system [30]. The magnitude of anisotropy is seen to closely follow the trend of dot separation as the barrier height is varied. This coincides with the intuitive picture presented in [24] where the source of anisotropy is attributed to the opposite rotation of the two electrons in spin-orbit fields directed along the respective momentum vectors, as the electrons tunnel across the barrier in opposite directions. As the dot separation becomes wider, tipping angle of the spins with respect to spin-orbit axis increases leading to higher anisotropic terms in the effective spin Hamiltonian. The energy scales for different spin-spin interactions in equation 3.4 calculated using effective interaction method are plotted as a function of barrier gate voltage V_3 in Appendix C.2.

An analytical calculation of J was performed using Heitler-London (HL) method by Kaveh Gharavi. The results of HL method predicted an exponential decrease in the isotropic J^{HL} (Fig. 3.3a) with barrier height in the well-separated regime, in qualitative agreement with the exact numerical method; however, the values for J^{HL} were about an order of magnitude larger than J. For low values of the barrier potential, the inter-dot separation becomes small and the assumption that the two-particle wavefunction can be written in terms of single-particle wavefunctions used in HL approximation, begins to break down. This is manifested as a sharp drop in the value of J^{HL} at $\mathrm{V}_3 = -0.25V$, and a prediction of a triplet ground-state for $\mathrm{V}_3 > -0.25V$. Such behaviour is known to be a signature of the breakdown of the Heitler-London approximation [81, 82]. The parameter β^{HL} shown in Fig. 3.3b yields a result similar to that found in [30]. This led to the conclusion that the Heitler-London method is not suitable for extracting the first-order anisotropic exchange parameter.

In the next section, we proceed to study the spin dynamics of the two electron system. The condition of adiabatic evolution inherent in the use of an effective spin Hamiltonian for describing the dynamics of a low energy subspace requires a large separation Δ_{orb} of the subspace from spatially excited states. The energy gap $\Delta_{orb} = \frac{\hbar^2\pi^2}{2m^*{a_B}^2}$ calculated within our numerical framework varies from 1 meV in the low barrier regime where the quantum wells are shallow to 2 meV at high barrier where the quantum wells are deeper. Keeping in mind the relevant energy scales, Zeeman energy E_Z, the exchange energy J, and the thermal energy kT a suitable range of gate operation can be found such that $\Delta_{orb} >> E_Z, J, k_BT$. This assists the adiabatic evolution of the system under fast switching of exchange interaction required for minimizing decoherence in resulting quantum gates.

3.3.2 Spin dynamics

In the following, we consider time evolution of selected states under a constant exchange Hamiltonian. The numerical methods developed here are well suited to simulating arbitrary voltage pulses; however for the purposes of testing the accuracy of effective spin Hamiltonians we restrict to the simplest case of a constant electrostatic potential.

The external magnetic field is chosen as $\boldsymbol{B} = (90\,\mathrm{mT})\hat{\boldsymbol{z}}$, a field compatible with EDSR experiments. We restrict attention to a set of initial states drawn from the S_0-T_0 Bloch sphere, $|S_0\rangle, |T_0\rangle, \frac{|S_0\rangle \pm |T_0\rangle}{\sqrt{2}}, \frac{|S_0\rangle \pm i|T_0\rangle}{\sqrt{2}}$. The time evolution of the spin state in the 4×4 Hilbert space under H_{spin} is given by $\rho_{spin}(t) = e^{-iH_{spin}t}\rho_{spin}(0)e^{iH_{spin}t}$. For a given value of V_3 (corresponding to exchange 'on'), we compare $\rho_{spin}(t)$ with the time-evolved density matrix in the full Hilbert space projected along the 4-dimensional basis $S = \{\xi_i\}_{i=\{1,..,4\}}$ described previously. The latter is calculated by numerically solving the time dependent Schrödinger equation for the 4-component spinor $\chi(t)$ as described in Sec 3.2. The elements of the

(non-normalized) projected density matrix are given by

$$\tilde{\rho}_{ij}(t) = \sum_{k,l=1,..,4} \langle \xi_k | \chi_i(t) \rangle \langle \chi_j(t) | \xi_l \rangle. \tag{3.22}$$

where $\chi_i(t)$ is the i^{th}-component of $\chi(t)$, and the tilde indicates that $\tilde{\rho}$ is not normalized. For non-zero SO coupling, in general $Tr(\tilde{\rho}) < 1$, indicating that information is lost by the projection to the low energy subspace. In order to compare with ρ_{spin}, we normalize this density matrix so that $\rho = \tilde{\rho}/Tr(\tilde{\rho})$. Fig. 3.4 shows the overlap between these states, $f = |Tr(\rho^\dagger \rho_{spin})|$, as a function of the evolution time. The time ranges from $0 \leq t \leq \frac{\pi\hbar}{4J}$, where J is the isotropic exchange energy for the same gate voltage but in the absence of SO coupling; the maximum time therefore corresponds to a SWAP gate in the case of isotropic exchange, $U_{swap} = \exp\left(-i\frac{\pi}{4}\hbar(\boldsymbol{\sigma}_1.\boldsymbol{\sigma}_2)\right)$. The initial state is $\frac{|S_0\rangle + |T_0\rangle}{\sqrt{2}}$ in the 4×4 Hilbert space, and the corresponding state $\psi_S(r_1, r_2)|S_0\rangle + \psi_{AS}(r_1, r_2)|T_0\rangle$ in the full Hilbert space. The central barrier gate voltage is set to $\mathrm{V}_3 = -0.55\,\mathrm{V}$ in this example, corresponding to $J = 0.041\,\mathrm{meV}$ and a SWAP gate time $\frac{\pi\hbar}{4J} = 12.6$ ps. Under the same conditions but with $|\boldsymbol{\eta}| = 15\,\mathrm{meV.nm}$, $J' = 0.035\,\mathrm{meV}$. In general, the isotropic exchange energy is reduced in the presence of SO coupling. This can be understood by the lowering of the energy gap between singlet and triplet states due to SO-induced mixing between these states.

Figure 3.4 shows that spin dynamics in the 4×4 Hilbert space under the H_{spin} of method A are in remarkably good agreement with the numerically exact results, for SO strengths up to $|\boldsymbol{\eta}| = 30$ meV.nm. We interpret the overlap f as a measure of the accuracy of the effective Hamiltonian, and conclude that the error per unit SO coupling is at most of the order 7×10^{-5} meV^{-1} nm^{-1} corresponding to the error seen at the largest value of SO coupling used in these numerical experiments, $|\boldsymbol{\eta}| = 45$ meV.nm. That is the key result of this work. By tracing the amplitude of each of the states $|S_0\rangle, |T_+\rangle, |T_0\rangle, |T_-\rangle$ during the exchange pulse, the agreement is also shown to hold good for each time during the pulse evolution. The rapid oscillations observed for the overlap f and in the probabilities pertaining to ρ result due to the fact that the input states chosen to be pure singlet/triplet states are actually superpositions which include highly excited states of the Hamiltonian H_{tot}. The amplitude of the oscillations increases with the size of the SO coupling strength as the overlap between the spin-orbit eigenstates of H_{tot} and the pure spin states decrease. The oscillations are removed if the input states are chosen to be the spin-orbit eigenstates.

Comparison of methods: In Fig. 3.5a we plot $f = |Tr(\rho^\dagger \rho_{spin})|$ at $t = \frac{\pi\hbar}{4J}$ versus the strength of the SO coupling, where ρ_{spin} is calculated by each of the methods A-D described above. The input state is the same as that of Fig. 3.4. Methods A-C match the numerically exact result far better than method D (truncation); even with SO coupling as large as $|\boldsymbol{\eta}| = 45\,\mathrm{meV.nm}$, methods A-C all agree to better than 5%, and method A better than 0.4%. Note that the methods A, C are based on the numerical solution of the complete Hamiltonian H_{tot} while methods B, D rely on the solutions of simpler spin-orbit free Hamiltonian, $H_{tot} - H_{SO}$.

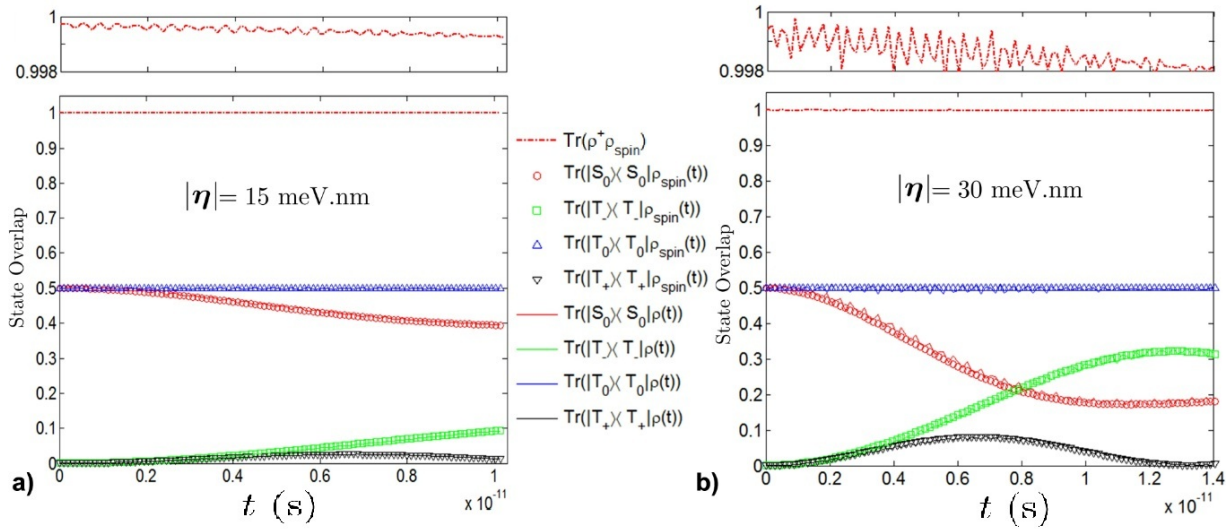

Figure 3.4: Plot of the overlap $f = |Tr(\rho^\dagger \rho_{spin})|$ between output states ρ_{spin} evolved under the H_{spin} of method A and the numerically exact results ρ obtained by solving the Schrödinger equation in the full Hilbert space. The timescale $t \in [0, \frac{\pi\hbar}{4J'}]$ is chosen to correspond to an approximate SWAP gate. The initial spin state is $\frac{|S_0\rangle+|T_0\rangle}{\sqrt{2}}$. The SO strength is in a) (15 meV.nm)$(\hat{\boldsymbol{x}}+\hat{\boldsymbol{y}})/\sqrt{2}$, and b) (30 meV.nm)$(\hat{\boldsymbol{x}}+\hat{\boldsymbol{y}})/\sqrt{2}$. The external magnetic field is set to $\boldsymbol{B} = (90\text{ mT})\hat{\boldsymbol{z}}$. We also plot the time evolution of probability densities of the spinors $Tr(|s\rangle\langle s|\rho(t))$, $Tr(|s\rangle\langle s|\rho_{spin}(t))$ where $s \in \{S_0, T_-, T_0, T_+\}$. Very good agreement is seen between the probabilities predicted by the two methods. The rapid oscillations seen in f and the probabilities pertaining to ρ result due to the fact that the input states chosen to be pure singlet/triplet states are superpositions which include highly excited states of the Hamiltonian H_{tot}.

Further, we carry out the comparison for different input states in order to identify any state dependent behavior. Figure 3.5b shows the result using method A for six different states on the S_0-T_0 Bloch sphere; here the SO coupling is set to $|\boldsymbol{\eta}| = 15\,\text{meV.nm}$. The error in the output states averages 1.2×10^{-5} for all inputs except $|T_0\rangle$, which is an eigenstate of H_{spin} when $\boldsymbol{\eta}$ is perpendicular to the spin quantization axis as in the current configuration (the error associated with this state indicates the level of numerical error in the FEM simulation). From these results we conclude that the effective interaction method (A) and the approximate Schrieffer-Wolf method (B) yield the most accurate spin dynamics in the presence of large SO coupling, noting that method C is fairly accurate but not sufficiently general.

Comparison with isotropic exchange: Finally, we apply our tool for studying unitary evolutions to quantify the fidelity between output states of the full dynamics in the presence of SO coupling, $\rho(t)$, and the output of an isotropic SWAP gate with zero SO coupling, ρ_{iso}. Fig. 3.6 shows the fidelity $f = |Tr(\rho^\dagger \rho_{iso})|$, where $\rho_{iso} = U_{swap}(\rho(0))U_{swap}^\dagger$ and $\rho(t)$ results from Eq. 3.22 with a pulse duration $t = \frac{\pi\hbar}{4J}$. The initial state $\rho(0)$ is again chosen as $\frac{|S_0\rangle + |T_0\rangle}{\sqrt{2}}$. The output state fidelity drops quickly as a function of the SO coupling strength. Since a leading-order SO effect is $J \to J' < J$, one could compensate by adjusting the pulse duration to be $t' = \frac{\pi\hbar}{4J'}$. This compensated case is also plotted (black points) for comparison. Surprisingly, the fidelity with the ideal isotropic gate is worse in the latter case, as the longer evolution time gives rise to larger error accumulation via the anisotropic terms. More sophisticated pulse designs will be required to correct for these anisotropies in the design of a high fidelity quantum gate.

3.3.3 Dependence of H_{spin} on experimental controls

Using method A to derive H_{spin}, we study the dependence of the exchange coefficients $\{J', \boldsymbol{\beta}, \gamma\}$ on the central barrier gate voltage V_3, external magnetic field $\boldsymbol{B}$, and spin-orbit vector $\boldsymbol{\eta}$. A finite magnetic field influences the exchange Hamiltonian through the modification of orbital states. Consider a magnetic field aligned perpendicular to the nanowire axis $\boldsymbol{B}_\perp = B_\perp \hat{\boldsymbol{z}}$. The vector potential $\boldsymbol{A}$ is chosen in the Landau gauge, $\boldsymbol{A} = (0, B_\perp x, 0)$ [83]. The effect of SO induced anisotropy in this case is to mix the exchange- and Zeeman-split singlet and triplet states. Fig. 3.7 shows the coefficients $\{J', |\boldsymbol{\beta}|, \gamma\}$ calculated using method A as a function of V_3 and as $B_\perp$ is varied from 0 to 2 T. Increasing the magnetic field strength enhances the dot confinement and lowers the interdot barrier height, pushing the electrons closer. This is reflected in a shift of the isotropic term J' towards higher values as $B_\perp$ is increased. Conversely, the anisotropic terms $\boldsymbol{\beta}, \gamma$ are suppressed for a strong $B_\perp$; the effect is clearly visible at more negative values of barrier gate voltage. The magnitudes of the exchange coefficients are independent of the direction of $\boldsymbol{B}_\perp$ in the $y - z$ plane by construction, since we use a 1D potential rather than the full 3D potential

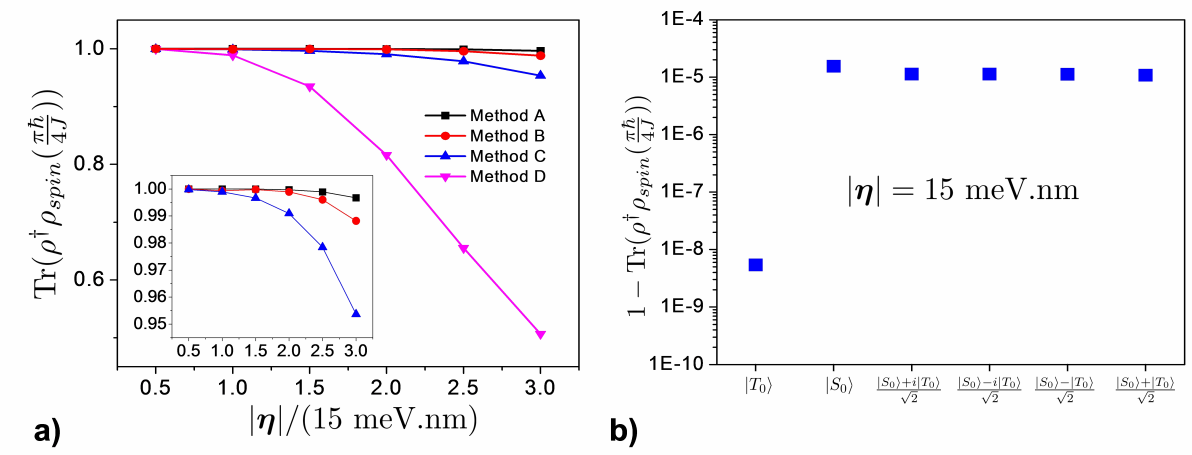

Figure 3.5: (a) Plot of $f = |Tr(\rho^\dagger \rho_{spin})|$ at $t = \frac{\pi\hbar}{4J}$ with anisotropic coefficients of H_{spin} calculated according to methods A-D over a range of spin-orbit coupling strengths $\boldsymbol{\eta} = |\boldsymbol{\eta}|(\hat{\boldsymbol{x}}+\hat{\boldsymbol{y}})/\sqrt{2}$. The initial state is $\frac{|S_0\rangle+|T_0\rangle}{\sqrt{2}}$. (b) $1-f$ calculated with method A for different input states on the S_0-T_0 Bloch sphere at $|\boldsymbol{\eta}| = 15\,\text{meV.nm}$.

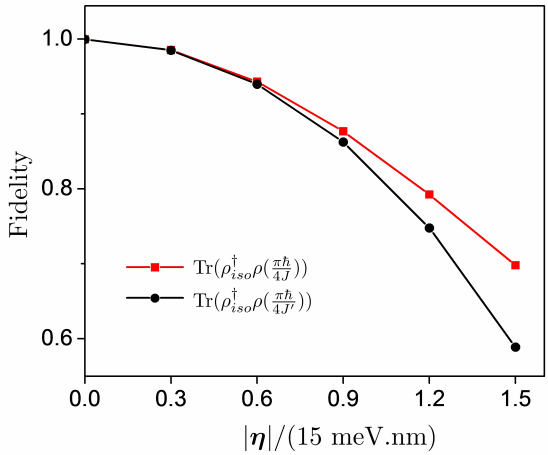

Figure 3.6: Here, we show a comparison between the output of the gates generated by isotropic and anisotropic exchange interaction. State fidelity (red dots) between outputs of an ideal isotropic SWAP gate, ρ_{iso}, and the full Hilbert space state evolution in the presence of SO coupling, $\rho(\frac{\pi\hbar}{4J})$, as a function of SO coupling strength $|\eta|$. The initial state is $\frac{|S_0\rangle+|T_0\rangle}{\sqrt{2}}$. The black dots correspond to $\rho(\frac{\pi\hbar}{4J'})$, where J' is the isotropic exchange energy in the presence of SO coupling.

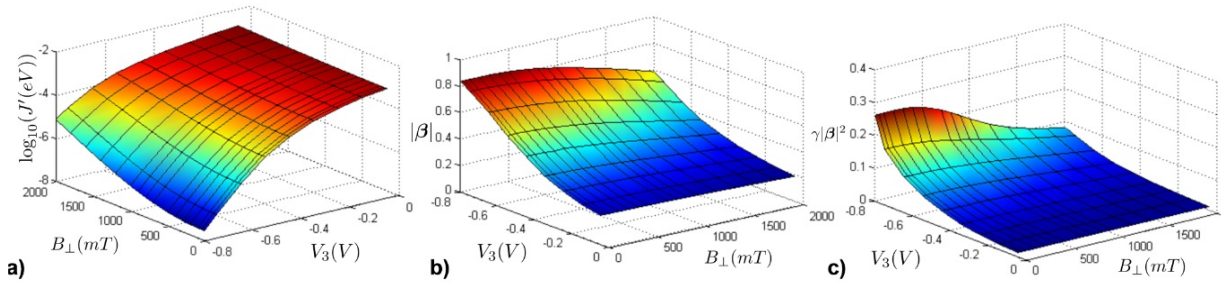

Figure 3.7: Calculated value of coefficients a) J', b) $|\boldsymbol{\beta}|$, c) γ using method A are plotted versus the central barrier voltage V_3 and the strength of external magnetic field $\boldsymbol{B}_\perp$. Here, $\boldsymbol{B}_\perp$ is along $\hat{\boldsymbol{z}}$ and the nanowire is along $\hat{\boldsymbol{x}}$, with the SO vector $\boldsymbol{\eta} = (15\,\text{meV.nm})(\hat{\boldsymbol{x}}+\hat{\boldsymbol{y}})/\sqrt{2}$. The parameter magnitudes are independent of the direction of $\boldsymbol{B}_\perp$ in the $y-z$ plane (due to the 1D approximation), and of the direction of $\boldsymbol{\eta}$ in the $x-y$ plane. The vector $\boldsymbol{\beta}$ aligns with $\hat{\boldsymbol{\eta}}$.

to describe the double dot.

On the other hand, an external magnetic field aligned with the dot axis, $\boldsymbol{B}_\parallel$, leaves the orbital states unchanged. The interplay between Zeeman and SO interactions [30] seen in the unitarily transformed basis (cf Sec. 3.2.2) is absent since the Zeeman Hamiltonian is always diagonal in the singlet-triplet basis (the direction of $\boldsymbol{B}$ defines the spin quantization axis.). Therefore, the magnitudes of anisotropic coefficients are independent of the orientation of the SO vector $\boldsymbol{\eta}$ with respect to the Zeeman field $\boldsymbol{B}$; however, $\hat{\boldsymbol{\beta}}$ aligns with $\hat{\boldsymbol{\eta}}$. This behaviour is expected since $\boldsymbol{\beta}$ is first-order in SO coupling, and should respond linearly to changes in $\boldsymbol{\eta}$.

Finally, we study the dependence of exchange coefficients on the strength of SO coupling $|\boldsymbol{\eta}|$. Fig. 3.8 shows a surface plot of the $\{J', \boldsymbol{\beta}, \gamma\}$ as a function of V_3 over a range of SO interaction strength $0 < |\eta| < 22\,\text{meV.nm}$, with external magnetic field $B_\perp = 90$ mT. Figures 3.8b and c show approximately linear and quadratic dependences on $|\boldsymbol{\eta}|$ for the first- and second-order terms, respectively.

A possible energy spectroscopy method for experimentally calculating the strength of SO coupling $|\boldsymbol{\beta}|$ is included in Appendix C.3.

3.4 Qubit Preparation and Measurement

The effective Hamiltonian construction that we described above is associated with a particular choice of pure spin basis states in which the SO induced spin-space correlations are assumed to be decoupled in the initial state of the system. However, there are no

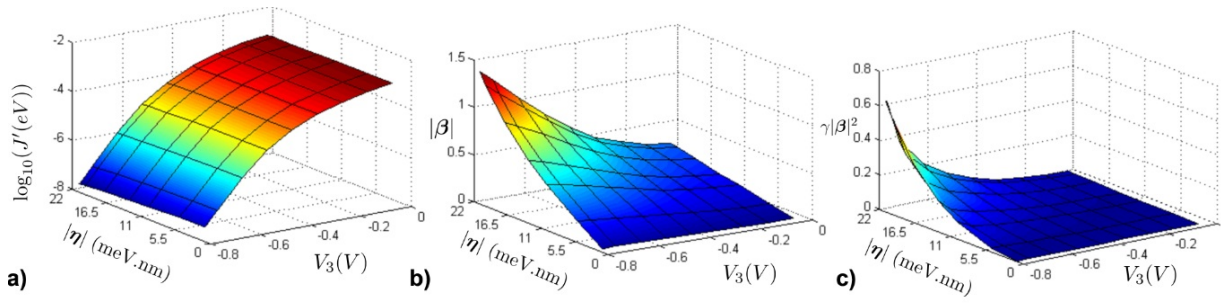

Figure 3.8: Calculated value of exchange coefficients a) J', b) $|\boldsymbol{\beta}|$, c) γ extracted after applying method A on the result of FEM simulation of time independent Schrödinger equation, are plotted versus the central barrier voltage V_3 and the strength of spin-orbit interaction $|\boldsymbol{\eta}|$. Here, the direction of $\boldsymbol{\eta}$ is $\hat{\boldsymbol{\eta}} = (\hat{\boldsymbol{x}}+\hat{\boldsymbol{y}})/\sqrt{2}$ and there's an external magnetic field $\boldsymbol{B} = (90\text{ mT})\hat{\boldsymbol{z}}$. The coefficients do not show a dependence on the direction of $\boldsymbol{B}$ in the $y-z$ plane. The magnitude of the first order term $\boldsymbol{\beta}$ shows a linear dependence on $|\boldsymbol{\eta}|$, and the vector $\boldsymbol{\beta}$ is aligned with $\hat{\boldsymbol{\eta}}$. The second order term shows an expected quadratic dependence on $|\boldsymbol{\eta}|$.

straightforward experimental procedures that can implement this decoupling to yield a state separable in spin and space components. The error associated with the initialization can become a hurdle in the achievement of high fidelity quantum operations. We are presently studying the generalization of effective spin Hamiltonian H_{spin} described above to a pseudo-spin subspace spanned by two electron SO-eigenstates in the regime that the exchange is negligible. As outlined in the DiVincenzo criteria, the choice of basis for encoding qubits in a QIP scheme is guided by the feasibility of both preparation and measurement of quantum state in such basis. Consider the state of the double well system before the exchange interaction is switched on. The two electrons are localized in separate quantum wells. In the presence of spin-orbit coupling, the eigenstates of an individual electron are spatial admixtures represented by two-component spinors

$$\begin{aligned} |\tilde{\uparrow}\rangle &= \zeta_1(r)|\uparrow\rangle + \zeta_2(r)|\downarrow\rangle, \\ |\tilde{\downarrow}\rangle &= \zeta_2^*(r)|\uparrow\rangle - \zeta_1^*(r)|\downarrow\rangle, \end{aligned} \tag{3.23}$$

satisfying $\langle\tilde{\uparrow}|\tilde{\downarrow}\rangle = 0$, where r is the spatial coordinate of the electron, $\zeta_i(r) \in L_2(\mathbb{C})$. By encoding the qubits in the pseudospins $\{|\tilde{\uparrow}\rangle, |\tilde{\downarrow}\rangle\}$, we can drop the requirement of performing local rotations for initialization in the pure spin basis. If the coupled quantum gates are performed adiabatically then it is guaranteed that the final state of the system will evolve back into the basis of these SO eigenstates. Towards this end, we are currently studying the construction of effective spin Hamiltonian in the spin-orbit eigenbasis in the regime of weak inter-dot coupling utilizing the effective interaction method studied above. The model space basis is redefined as

$$\{\tilde{\xi}_j\}_{j=1-4} = \{\tilde{S}_0, \tilde{T}_-, \tilde{T}_0, \tilde{T}_+\}, \tag{3.24}$$

where

$$|\tilde{S}_0\rangle = \frac{|\tilde{\uparrow}\tilde{\downarrow}\rangle - |\tilde{\downarrow}\tilde{\uparrow}\rangle}{\sqrt{2}}, \quad |\tilde{T}_-\rangle = |\tilde{\downarrow}\tilde{\downarrow}\rangle, \quad |\tilde{T}_0\rangle = \frac{|\tilde{\uparrow}\tilde{\downarrow}\rangle + |\tilde{\downarrow}\tilde{\uparrow}\rangle}{\sqrt{2}}, \quad |\tilde{T}_+\rangle = |\tilde{\uparrow}\tilde{\uparrow}\rangle. \tag{3.25}$$

The eigenstates of H_{tot} at a different height of the barrier when expressed in the basis of Eq. 3.24 produces the operator V in Eq. 3.11 leading to the construction of desired H_{spin} using Eq. 3.12. The form of the resulting Hamiltonian is not known apriori. However, the off-diagonal elements will still appear in H_{spin} due to a mismatch between the quantization axes at different barrier heights. The direction of quantization axis is determined both by the external Zeeman field and the internal spin-orbit fields that depend on the spatial wavefunction. Further, it is noted that the EDSR mechanism utilized for implementing single qubit gates produces transitions between the pseudo-spin states $\{\tilde{\uparrow}, \tilde{\downarrow}\}$ rather than the true spins [84]. The analysis of gate operation in the basis of spin-orbit eigenstates will present a more well-rounded approach to QIP in our nanowire double dot device. This is an ongoing topic of study.

3.5 Summary

In this chapter we have developed numerical methods to accurately describe spin dynamics in gate-defined double quantum dots formed in a 1D quantum wire in the presence of a large SO interaction. The form of the SO coupling is chosen to be appropriate for a quasi-1D nanowire. Starting with a 3D model of a nanowire sitting atop local gate electrodes, we iteratively solved the Poisson-Schrödinger equations for the 3D electrostatic potential, which was projected to a 1D potential to numerically solve for the double dot eigenstates and spectrum. The model allows for an arbitrary external magnetic field, and arbitrary strength and direction for the SO coupling. A 4×4 effective spin Hamiltonian H_{spin} was calculated from the eigensolutions using an effective Hamiltonian method. H_{spin} has the form of anisotropic exchange and is expressed in the separable basis of singlet and triplets. Once H_{spin} is determined as a parametric function of gate voltage, the spin dynamics under arbitrary gate voltage sequences can be calculated. By comparison with the computationally expensive, numerically exact evolution in the full Hilbert space, we find the spin dynamics under H_{spin} to be very accurate, even up to relatively strong SO coupling strengths. We investigated the parametric dependence of exchange coefficients on central barrier gate voltage, external magnetic field, and SO strength. The effect of a magnetic field perpendicular to the nanowire axis is to influence the exchange coefficients through increasing the confinement and reducing dot separation. The dependence of exchange coefficients on perpendicular magnetic field becomes more pronounced at larger interdot barrier height. The direction associated with the SO coupling determines the first-order anisotropy direction $\hat{\boldsymbol{\beta}}$, and the magnitudes of the first- and second-order terms scale roughly linearly and quadratically with $|\boldsymbol{\eta}|$, respectively.

We believe the numerical framework established here is sufficiently general and flexible to accurately simulate spin dynamics over a wide range of experimentally accessible conditions. It can guide experiments to measure the exchange coefficients that determine H_{spin}, and can be used to predict spin dynamics as a function of the control parameters directly accessible to experiment: local gate voltages and external magnetic field. In future work, we would like to perform a similar study of H_{spin} and spin dynamics in the basis of SO eigenstates. This is a natural basis in which the electron spins in quantum dots are thermally initialized. The EDSR induced single spin operations are also performed in this coupled spin-space basis which makes it a suitable choice for QIP. It will also be relevant to calculate the effect of the local gate voltages on the Rashba spin-orbit coupling by considering the long-rage variations in the 3D electrostatic potential prior to the projection to 1D. One drawback of the current method is the 1D approximation which renders the problem cylindrically symmetric, in contrast to the real device, whose cylindrical symmetry is broken by the device geometry. However, due to the small effective mass of electrons in InAs, the constant-$\boldsymbol{\eta}$, 1D approximation should be reasonably accurate for nanowires of sufficiently small diameter, particularly as a heuristic guide for experiments.

Chapter 4

Conclusions

In the past few years there has been an extensive research on InAs nanowires inspired by the prospects of discovering new physics in the low-dimensional geometry of nanowires [85, 86, 87] as well as developing technological applications ranging from nanoscale circuits [38] and gas sensors [39] to high-efficiency solar cells [40]. Motivated by the goal of building spin based QIP device using InAs nanowires, we addressed two open problems in the field. We used numerical modelling of realistic nanowires devices to, i) characterize and explain experimentally observed electron transport in InAs nanowire FET devices, ii) develop a framework for designing two qubit coupled quantum gates in a lab experiment. Both the problems addressed in this thesis serve the purpose of bridging the gap between theory and physical implementation of a prototypical QIP device based on InAs nanowire double quantum dots.

The problem of nanowire transport introduced in section 1.1.1 has been answered in Chapter two. Based on a ubiquitous trend of experimentally observed temperature-dependent mobility, we hypothesized remote Coulomb scattering from ionized surface states as a limiting scattering mechanism for electron transport in InAs nanowires. In 2.3.1 we calculated Coulomb scattering rates from a simulated scattering potential of a surface distribution of positively charged donors for D=50 nm nanowire FET device. The key result of this work is illustrated in figure 2.9 which shows a reasonably good agreement between experimentally observed effective mobility and the mobilities calculated using modelled scattering rates. The model assumed a temperature dependence of surface donor state ionization in line with the observed increase in experimental carrier concentration with temperature. Inspite of the fact that the model is relatively simple, it adequately incorporates the main factors governing the carrier relaxation rate. A characterization like this for quasi-1D nanowire is useful for the future study of nanowires as the radii get smaller and the interplay of confinement and surface effects dominate transport. The dependence of scattering rate on nanowire radii remains to be investigated within our model. The nanowire surface to volume ratio increases for smaller diameter which leads us to expect stronger overlap of electron wavefunction with nanowire surface resulting in stronger scattering

rates. This is what we also observe experimentally. On the other hand, smaller diameter leads to wider separation of the 1-D subbands, thereby, suppressing the inter-band scattering. It will be interesting to see if a somewhat similar temperature dependence of surface donor ionization is able to expain the scale as well as the reduced slopes of experimental mobility seen for smaller radii nanowires.

The second problem concerning the design of coupled quantum gates has been addressed in Chapter three. The presence of large spin-orbit interaction in InAs leads to coupling between spin and spatial coordinates of the electron preventing the diagonalization of double well Hamiltonian in the spin basis. We reduced the complete Hilbert space interactions of a spin-orbit coupled qubit to an effective 4×4 Hamiltonian acting in the spin space employing techniques borrowed from different fields of study. We tested the accuracy of derived effective Hamiltonian by direct comparison with the exact numerical simulation of time dynamics of Schrödinger equation for the spin orbit coupled system. Figure 3.5 is the key result illustrating the high degree of agreement obtained between the dynamics generated by effective spin Hamiltonian and the time-dependent Schrödinger equation solved in complete Hilbert space of the system. The effective Hamiltonian was paramterized by a set of variables $J', \boldsymbol{\beta}, \gamma$. An operational characterization of this interaction was performed for experimentally accessible control parameters: gate voltages, external magnetic field, strength and direction of spin orbit vector. Within the numerical framework, we were able to treat a spin-orbit coupling of arbitrary strength on equal footing with other interactions in the Hamiltonian.

The study of effective spin Hamiltonian in the pseudo-spin basis (eq. 3.9) is in progress. The strength of anisotropic terms in the Hamiltonian are suppressed in the pseudo-spin basis. By construction, H_{spin} is diagonal at the start of the pulse; on shifting to a different gate voltage the off-diagonal terms appear only in the presence of an external magnetic field. For future work, it might be of interest to perform following numerical experiments with the setup already available: a complete study of single spin dynamics in a gated 3-D quantum dot under the influence of an oscillating electric field in an EDSR like setup using a PDE based Comsol model. This could be potentially useful for studying the parameters of a single qubit gate design as well as for the study of error mechanisms in the gate. Also, the double dot numerical model can be utilized to calculate the SO induced error probabilities in a Pauli spin blockade experiment by studying spin dynamics in the presence of electrical detuning between the quantum wells.

Appendix

APPENDICES

Appendix A

Stacking faults and mobility

A.1 Structural Defects

The relationship between structure and mobility was investigated by performing post-measurement transmission electron microscopy (TEM) on selected devices by Yipu Song; this was motivated by the observation that a fraction of devices displayed significantly lower mobilities than were typical for a given nanowire diameter. Indeed, it was observed that a 55 nm diameter nanowire with low mobility $\sim 1,000$ cm^2/Vs had a high linear density of stacking faults, at least $\sim$(70 nm)$^{-1}$ as shown in figure A.1. In contrast, the highest mobility device we measured, device 1, had no visible faults along the entire channel length. Device 3 ($D = 35$ nm) was found to have only one visible fault as shown in figure A.1, and better mobility than the $D = 55$ nm device, despite having a smaller diameter. The magnitude and temperature dependence of mobility appear to be greatly reduced in the D = 55 nm device due to the high density of stacking faults. Wurtzite InAs has a 20% larger bandgap than zincblende InAs [88], so that for electrons, stacking faults correspond to potential wells that may be as deep as $\sim$ 70 meV. Since these are planar defects, the reflection coefficient for an incoming plane wave can be a sizable fraction of unity. On the other hand, we cannot obtain theoretical mobilities as low as $\sim 1000\,\mathrm{cm}^2/Vs$ from a simple 1D model of square well potentials at the linear defect density observed here. Further investigation is required to clarify the origin of the surprisingly low mobilities seen here.

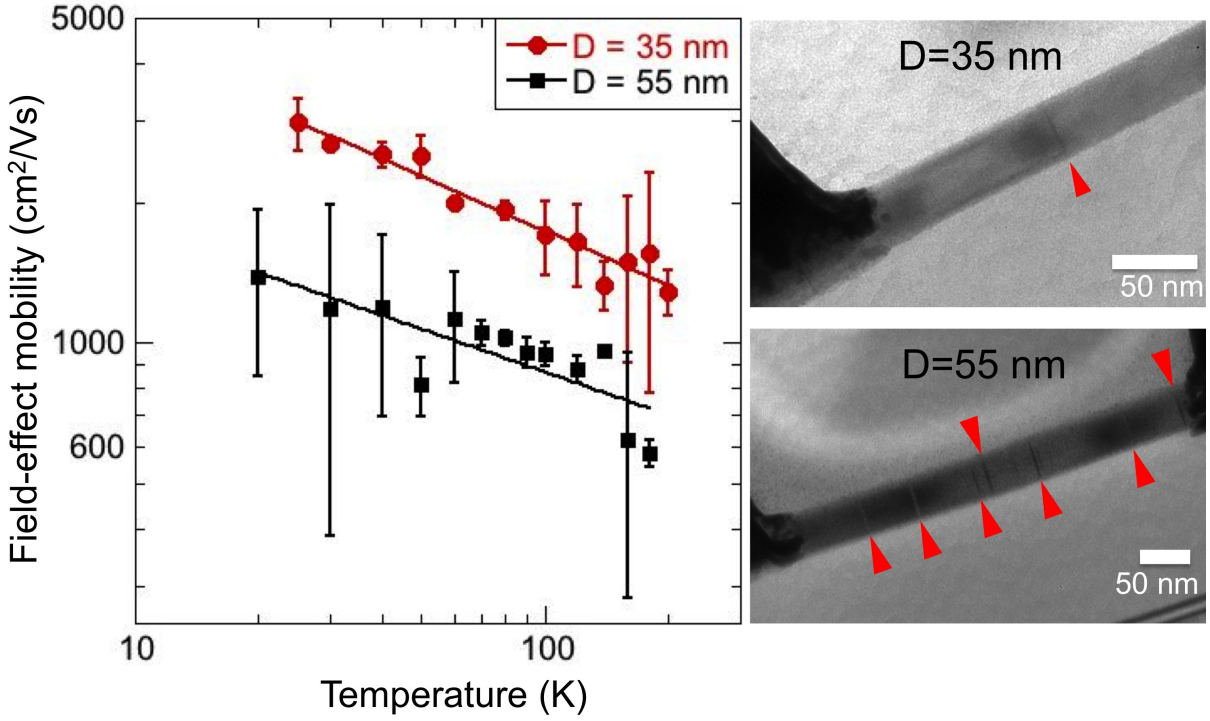

Figure A.1: Stacking fault density and reduced mobility. Experimental mobilities (left) and post-measurement TEM images (right) for device 3 ($D = 35$ nm) and a low-mobility $D = 55$ nm nanowire FET device. Stacking faults are indicated by the red arrows; at least 7 faults can be seen in the $D = 55$ nm nanowire, compared to only one visible fault in the $D = 35$ nm nanowire. The nanowires are imaged along the [-2 1 1 0] zone axis so that all planar defects will be visible. The solid lines show power law fits to $T^{-0.4}$ and $T^{-0.3}$ for the 35 nm and 55 nm devices, respectively. No faults were observed along the entire channel for device 1 ($\langle D \rangle = 71$ nm).

Appendix B

Numerical Solvers

Geometry of the prototype nanowire device is shown in figure B.1. The bottom layer comprises a SiO_2 dielectric layer and is in direct contact with the metallic gate at the bottom surface serving as the global back gate. InAs nanowire is placed on top of the SiO_2 layer and is assumed to be embedded inside a volume with dielectric constant $\epsilon_r = 1$. The model domain is meshed by tetrahedral volume elements. A geometry dependent mesh size is applied by Comsol® that renders finer mesh elements within the nanowire volume.

The Poisson equation below is solved using the electrostatics module of Comsol Multiphysics.

$$\nabla.(\epsilon_0 \epsilon_r \boldsymbol{E}) = \rho_v \tag{B.1}$$

$$\boldsymbol{E} = -\nabla V \tag{B.2}$$

The boundary conditions used in the Comsol FEM model are as follows.

- *Dirichlet boundary condition:* $V = 0$ at the bottom surface of the SiO_2 layer, $V = 0$ at all the boundaries (interior as well as exterior) of source and drain contacts at the ends of the nanowire.
- *Neuman boundary condition:* $\rho_s = e\sigma_{ss}^{+}$ along the InAs nanowire surface. This specifies the value of electric displacement field($\boldsymbol{D}$) component perpendicular to the nanowire surface $\boldsymbol{n}.(\boldsymbol{D}_1 - \boldsymbol{D}_2) = \rho_s$.
- *Charge conservation for all domains.*
- *Space charge density:* $\nabla.\boldsymbol{D} = \rho_v$ specified inside nanowire volume as calculated from the solution of Schrödinger equation.
- *Electric displacement field:* $\boldsymbol{n}.\boldsymbol{D} = \boldsymbol{n}.\boldsymbol{D}_0$ in the plane of source-drain surfaces, where $\boldsymbol{D}_0 = 0$ is the boundary electric displacement field.

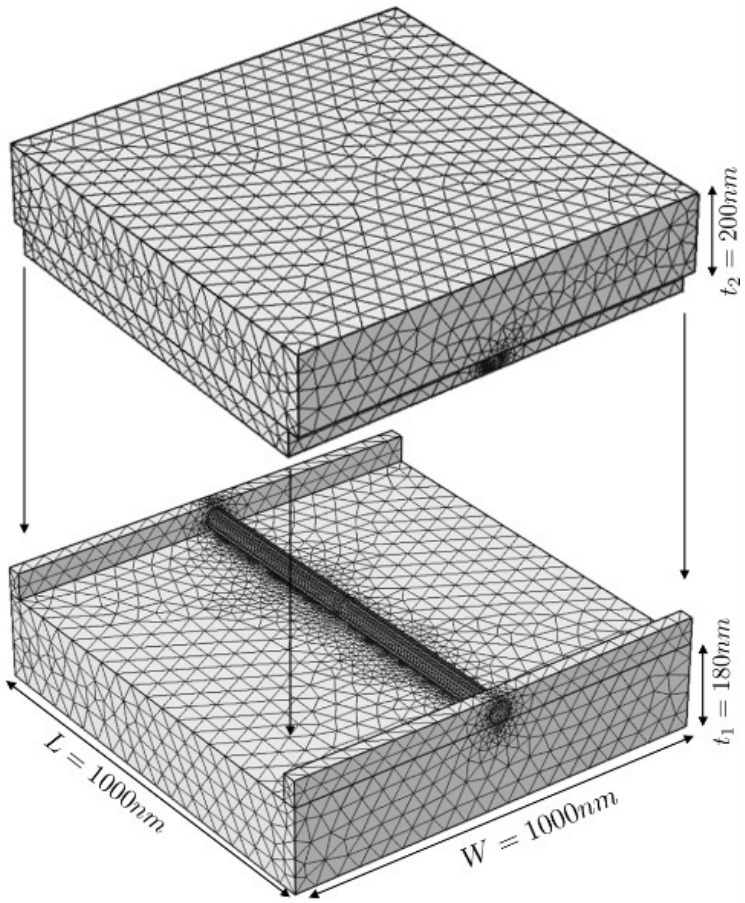

Figure B.1: Model domain for Poisson solver showing tetrahedral mesh elements and variable mesh sizes for different components: nanowire, dielectric substrate and surrounding vacuum.

The two-dimensional Schrödinger equation is solved for a nanowire cross-section. Instead of using the Dirichlet boundary condition at the circumference a potential well of height equal to the electron affinity in InAs, $E_a = 4.9$ eV is specified at the boundary. The coupling between Poisson and Schrödinger solvers is enabled through the use of Comsol interpolation function definition that allows passing the stored solutions $V(x, y, z), n(x, y, z)$ as inputs in the respective models.

The Poisson solver described above is modified for the study of gate controlled exchange coupling discussed in Chapter 3. In addition to the global back-gate, a set of five local gates of width 20 nm and pitch 60 nm are added to the device geometry as shown in figure 3.1. A negative voltage applied at the gates 1 and 5 confines the electron, a positive voltage applied at gates 3 and 4 (plunger gates) creates a potential well while the central gate barrier is set to a variable negative gate voltage. The local gate voltages are specified

as additional Dirichlet boundary conditions in the model. This Poisson solver is coupled with a 3-D Schrödinger solver defined over a cylindrical nanowire of diameter D=50 nm and length L=1000μm. The solver includes the kinetic and potential energy terms but not the electron-electron or spin-orbit interaction. The converged potential solution is axially projected to one-dimension and then used as an input in a second Schrödinger solver for obtaining spin-orbit eigen solutions for H_{tot} described in the main text.

The time-independent Schrödinger equation $H|\chi\rangle = E|\chi\rangle$ is specified as a system of coupled linear PDEs using the Comsol coefficient form PDE interface for four dependent variables $\{\phi_{S0}, \phi_{T-}, \phi_{T0}, \phi_{T+}\}$ over a 2-D square domain. The electrostatic interaction term, external potential term as well as Zeeman term appear in the matrix for absorption coefficient a, the spin-orbit interaction appear in the matrix for convection coefficient β while the kinetic energy term resembles the diffusion term in the coefficient form PDE. The boundary condition $|\chi\rangle$=0 is applied at all edges.

A constraint corresponding to the anti-symmetry condition for spatial component of the triplet states is added to the Comsol study as $\int_0^L \int_0^L \phi_s(r_1, r_2)\phi_s^\dagger(r_1, r_2)dr_1dr_2 = 0$ where $s \in \{T_0, T_-, T_+\}$. The spatial component of singlet is constrained as $\int_0^L \int_0^L \phi_{S_0}(r_1, r_2)\phi_{S_0}^\dagger(r_1, r_2)dr_1dr_2 = 2\int_0^L \int_0^{r_1} \phi_{S_0}(r_1, r_2)\phi_{S_0}^\dagger(r_1, r_2)dr_1dr_2$. The solver domain is meshed by 2-D triangular elements with an edge length of $h < 10$ nm using 'advancing front' triangulation method. A stationary study is performed using Comsol's default eigenvalue solver with a specified relative tolerance of 10^{-15} for the computed eigenvalues.

The simulation of time-dependent Schrödinger equation 3.8 is carried out on the same model using Comsol's time dependent solver. The stepping method used is a variable order BDF (backward differentiation formula) with maximum order 5. For the specified tolerance of 10^{-3}, this produces time steps of length $\Delta t = 10^{-16}$ s for simulating a pulse of length $t \sim 10$ ps. The alternative 'generalized alpha' method while producing faster convergence gives erroneous results and is not found suitable for our study.

For the purposes of parametric studies as well as automation, the comsol models were combined with Matlab interface using Comsol LiveLink with MATLAB utility for scripting usage.

Appendix C

Appendix to Chapter 3

C.1 Comments on Method C: Parametric fitting of eigenvalues

In the absence of magnetic field, the eigenstates of effective spin Hamiltonian given by equation 3.4 are doubly degenerate. As such the value of three unknowns $\{J', |\boldsymbol{\beta}|, \gamma\}$ and a constant can not be obtained from the solution of three algebraic equations. In this case, we determine $|\boldsymbol{\beta}|$ from the spin-orbit eigenstates, noting that $|\langle \tilde{T_-}|S_0\rangle|^2 = (\frac{\sqrt{1+|\boldsymbol{\beta}|^2}-1}{|\boldsymbol{\beta}|})^2$ where $|\tilde{T_-}\rangle$ refers to the spin-orbit modified triplet state. The remaining parameters are then obtained using the energy eigenvalues.

The method produces erroneous results in the regime $E_Z > J$. An expected reason for the breakdown is the increased interaction between the $|T+\rangle$ and higher spatial orbital states due to the reduction of corresponding energy gap in high magnetic fields.

C.2 SO coupling in zero magnetic field

In this section, we provide additional details on the numerical eigenspectrum and eigenstates obtained for the two-electron double well system. In figure C.1a, the energy scales of different terms in the effective spin Hamiltonian are plotted in zero external field, $\boldsymbol{B} = 0$. Figure C.1b shows the projection of spin-orbit eigenstates along the basis of unperturbed states $\{\xi_j\}_{j=1,..,4}$. The triplet degeneracy in the absence of magnetic field is seen to be lifted by the spin-orbit interaction. The eigenstates of the Hamiltonian are hybridized over the triplets irrespective of the strength of spin-orbit interaction.

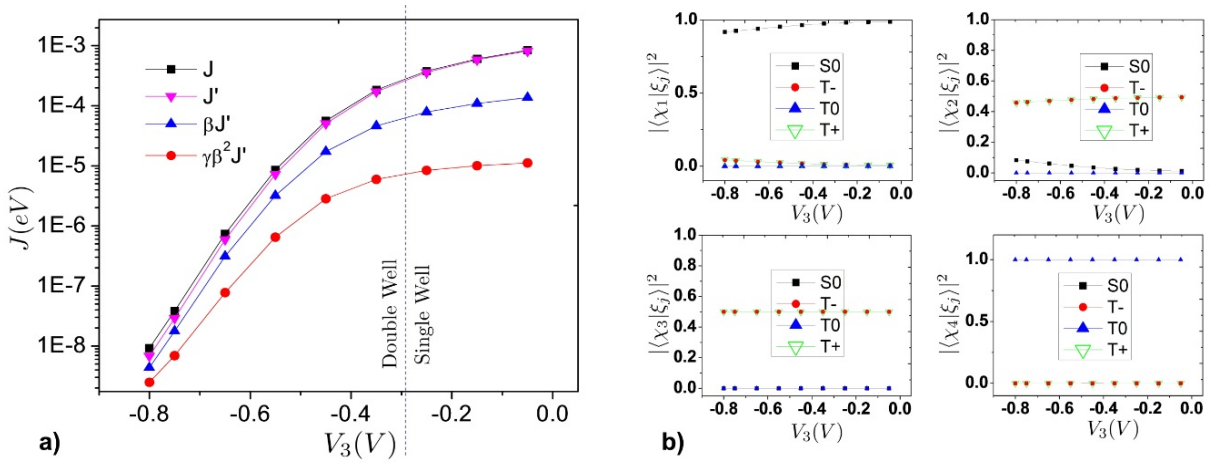

Figure C.1: a) Plot showing the energy scale of different terms in the effective spin Hamiltonian Eq. (3.4) as a function of central barrier height V_3. The values are extracted from the FEM simulation using method A in zero external field $\boldsymbol{B} = 0$, b) Projection of the lowest 4 spin-orbit eigenstates $\chi_i(r_1, r_2), i = \{1, 2, 3, 4\}$ along the basis of unperturbed singlet-triplet states, $S = \{\xi_j\}_{j=1,..,4}$. Mixing between singlets and triplets increases in the regime where electrons are further apart.

C.3 Energy spectroscopy of SO coupling strength

In figure C.2 we plot the energy gap between singlet and triplet states in the presence of external Zeeman coupling at a point V_3 such that $E_Z \sim J$. This energy gap is amplified by the spin-orbit coupling and can possibly be used in an energy spectroscopy scheme to measure the strength of SO coupling.

C.4 Matrix for SO Hamiltonian

The spin-orbit Hamiltonian in eq. 3.6 can be written down in the basis $\{\xi_j\}_{j=1-4}$ introduced in eq. 3.9 as below

$$H_{SO_j} = \frac{-i\hbar}{\sqrt{2}} \begin{bmatrix} 0 & (\alpha_D - i\alpha_R)\partial r_j & 0 & -(\alpha_D + i\alpha_R)\partial r_j \\ (\alpha_D + i\alpha_R)\partial r_j & 0 & (\alpha_D + i\alpha_R)\partial r_j & 0 \\ 0 & (\alpha_D - i\alpha_R)\partial r_j & 0 & (\alpha_D + i\alpha_R)\partial r_j \\ (-\alpha_D + i\alpha_R)\partial r_j & 0 & (\alpha_D - i\alpha_R)\partial r_j & 0 \end{bmatrix}$$

where $j = \{1, 2\}$, $\alpha_R = \eta_x, \alpha_D = \eta_y$ are the coefficients of Rashba and Dresselhaus interaction terms, respectively.

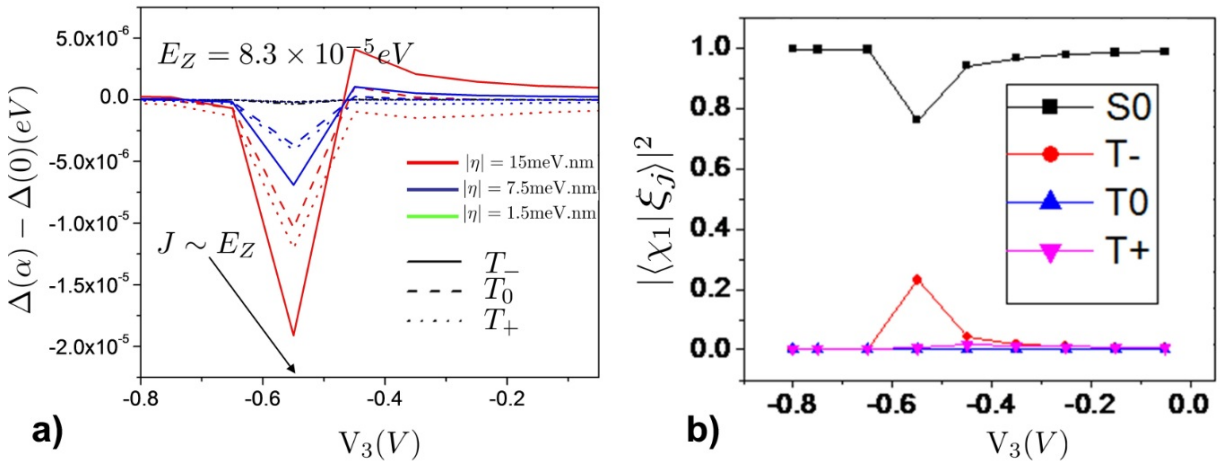

Figure C.2: a) Plot of $\Delta(\alpha) - \Delta(0)$, where $\Delta_i(\alpha) = E_{S0}(\alpha) - E_{T_i}(\alpha), i = \{+, 0, -\}$. The notation $E_s(\alpha)$ refers to the energy of spin state s when $|\eta| = 15\,\text{meV.nm}$. Plot shows spin-orbit induced energy shifts between triplet-singlet level splittings in $B_\perp = 90\,\text{mT}$ for three different values of spin orbit strength, $|\eta| \in \{15, 7, 1.5\}\,\text{meV.nm}$, b) Projection of the spin-orbit eigenstate $|\langle\chi_1|\xi_j\rangle|^2_{j=\{1,..,4\}}$ along the spin states showing spin-orbit induced mixing between $|S0\rangle$ and $|T-\rangle$ states in a spin-orbit eigenstate as a function of barrier height V_3.

Bibliography

[1] Schroer, M. D., Jung, M., Petta, J. R. Phys. Rev. Lett. 2011,**107**, 176811.

[2] M. T. Björk, A. Fuhrer, A. E. Hansen, M. W. Larsson, L. E. Fröberg, and L. Samuelson, "Tunable effective g factor in inas nanowire quantum dots," *Phys. Rev. B*, vol. 72, p. 201307, Nov 2005.

[3] M. P. Nowak, B. Szafran, F. M. Peeters, B. Partoens, and W. J. Pasek, "Tuning of the spin-orbit interaction in a quantum dot by an in-plane magnetic field," *Phys. Rev. B*, vol. 83, p. 245324, Jun 2011.

[4] C. Fasth, A. Fuhrer, M. T. Bjrk, and L. Samuelson, "Tunable double quantum dots in inas nanowires defined by local gate electrodes," *Nano Letters*, vol. 5, no. 7, pp. 1487–1490, 2005.

[5] A. Pfund, I. Shorubalko, R. Leturcq, and K. Ensslin, "Top-gate defined double quantum dots in inas nanowires," *Applied Physics Letters*, vol. 89, no. 25, p. 252106, 2006.

[6] D. DiVincenzo *et al.*, "The physical implementation of quantum computation," *arXiv preprint quant-ph/0002077*, 2000.

[7] P. W. Shor, "Scheme for reducing decoherence in quantum computer memory," *Phys. Rev. A*, vol. 52, pp. R2493–R2496, Oct 1995.

[8] A. Steane, "Error correcting codes in quantum theory," *Physical Review Letters*, vol. 77, no. 5, pp. 793–797, 1996.

[9] P. Shor, "Fault-tolerant quantum computation," in *Foundations of Computer Science, 1996. Proceedings., 37th Annual Symposium on*, pp. 56–65, IEEE, 1996.

[10] M. Nielsen and I. Chuang, *Quantum computation and quantum information*. Cambridge university press, 2010.

[11] D. Loss and D. P. DiVincenzo, "Quantum computation with quantum dots," *Phys. Rev. A*, vol. 57, pp. 120–126, Jan 1998.

[12] G. Burkard, D. Loss, and D. P. DiVincenzo, "Coupled quantum dots as quantum gates," *Phys. Rev. B*, vol. 59, pp. 2070–2078, Jan 1999.

[13] J. Petta, A. Johnson, J. Taylor, E. Laird, A. Yacoby, M. Lukin, C. Marcus, M. Hanson, and A. Gossard, "Coherent manipulation of coupled electron spins in semiconductor quantum dots," *Science*, vol. 309, no. 5744, pp. 2180–2184, 2005.

[14] G. Dresselhaus, "Spin-Orbit Coupling Effects in Zinc Blende Structures," *Physical Review*, vol. 100, pp. 580–586, Oct. 1955.

[15] I. Zorkani and E. Kartheuser, "Resonant magneto-optical spin transitions in zinc-blende and wurtzite semiconductors," *Phys. Rev. B*, vol. 53, pp. 1871–1880, Jan 1996.

[16] Y. A. Bychkov and E. I. Rashba, "Oscillatory effects and the magnetic susceptibility of carriers in inversion layers," *Journal of Physics C Solid State Physics*, vol. 17, pp. 6039–6045, Nov. 1984.

[17] C. Fasth, A. Fuhrer, L. Samuelson, V. N. Golovach, and D. Loss, "Direct measurement of the spin-orbit interaction in a two-electron inas nanowire quantum dot," *Phys. Rev. Lett.*, vol. 98, p. 266801, Jun 2007.

[18] A. Pfund, I. Shorubalko, K. Ensslin, and R. Leturcq, "Spin-state mixing in inas double quantum dots," *Phys. Rev. B*, vol. 76, p. 161308, Oct 2007.

[19] Ė. Rashba and G. Landwehr, *Landau level spectroscopy*. North-Holland, 1991.

[20] K. C. Nowack, F. H. L. Koppens, Y. V. Nazarov, and L. M. K. Vandersypen, "Coherent control of a single electron spin with electric fields," *Science*, vol. 318, no. 5855, pp. 1430–1433, 2007.

[21] S. Nadj-Perge, S. M. Frolov, E. P. A. M. Bakkers, and L. P. Kouwenhoven, "Spin-orbit qubit in a semiconductor nanowire," *Nature*, vol. 468, pp. 1084–1087, Dec. 2010.

[22] W. Heisenberg, "Zur theorie des ferromagnetismus," *Z. Phys.*, vol. 49, 2000.

[23] D. DiVincenzo, D. Bacon, J. Kempe, G. Burkard, and K. Whaley, "Universal quantum computation with the exchange interaction.," *Nature*, vol. 408, no. 6810, p. 339, 2000.

[24] K. V. Kavokin, "Anisotropic exchange interaction of localized conduction-band electrons in semiconductors," *Phys. Rev. B*, vol. 64, p. 075305, Jul 2001.

[25] S. Gangadharaiah, J. Sun, and O. A. Starykh, "Spin-orbit-mediated anisotropic spin interaction in interacting electron systems," *Phys. Rev. Lett.*, vol. 100, p. 156402, Apr 2008.

[26] A. Stephens and Z. Evans, "Accuracy threshold for concatenated error detection in one dimension," *Physical Review A*, vol. 80, no. 2, p. 022313, 2009.

[27] D. Stepanenko, N. E. Bonesteel, D. P. DiVincenzo, G. Burkard, and D. Loss, "Spin-orbit coupling and time-reversal symmetry in quantum gates," *Phys. Rev. B*, vol. 68, p. 115306, Sep 2003.

[28] G. Burkard and D. Loss, "Cancellation of spin-orbit effects in quantum gates based on the exchange coupling in quantum dots," *Phys. Rev. Lett.*, vol. 88, p. 047903, Jan 2002.

[29] L.-A. Wu and D. A. Lidar, "Universal quantum logic from zeeman and anisotropic exchange interactions," *Phys. Rev. A*, vol. 66, p. 062314, Dec 2002.

[30] F. Baruffa, P. Stano, and J. Fabian, "Theory of anisotropic exchange in laterally coupled quantum dots," *Phys. Rev. Lett.*, vol. 104, p. 126401, Mar 2010.

[31] S. A. Dayeh, "TOPICAL REVIEW: Electron transport in indium arsenide nanowires," *Semiconductor Science Technology*, vol. 25, p. 024004, Feb. 2010.

[32] G. Holloway, Y. Song, C. Haapamaki, R. LaPierre, and J. Baugh, "Trapped charge dynamics in inas nanowires," *arXiv preprint arXiv:1209.3237*, 2012.

[33] G. Holloway, Y. Song, C. Haapamaki, R. LaPierre, and J. Baugh, "Electron transport in inas-inalas core-shell nanowires," *arXiv preprint arXiv:1209.2767*, 2012.

[34] Dayeh, S. A.; Yu, E. T.; Wang, D. L. Nano Lett. 2009, **9**, 1967-1972.

[35] Schroer, M. D.; Petta, J. R. Nano Lett. 2010, **10**, 1618-1622.

[36] Joyce, H. J.; Wong-Leung, J.; Gao, Q.; Hoe Tan, H.; Jagadish, C. Nano Lett. 2012, **10**, 908-915.

[37] Dick, K. A.; Thelander, C.; Samuelson, L.; Caroff, P. Nano Lett. 2012, **10**, 3494-3499.

[38] Xiang, J.; Lu, W.; Hu, Y.J.; Wu, Y.; Yan, H.; Lieber, C. L. Nature 2006, **441**, 489-493.

[39] Du, J.; Liang, D.; Tang, H.; Xuan, P.A.; Gao, X. P. A. Nano Lett. 2009, **9**, 4348-4351.

[40] LaPierre, R. R. J. Appl. Phys. 2011, **109**, 034311.

[41] Suyatin, D. B.; Thelander, C.; Bjork, M. T.; Maximov, I.; Samuelson, L. Nanotechnology 2007, **18**, 105307.

[42] Ford, A. C.; Ho, J. C.; Chueh, Y. L.; Tseng, Y. C.; Fan, Z. Y.; Guo, J.; Bokor, J.; Javey, A. Nano Lett. 2009, **9**, 360-365.

[43] Nadj-Perge, S.; Frolov, S. M.; Bakkers, E. P. A. M.; Kouwenhoven, L. P. Nature 2010, **468**, 1084.

[44] Baugh, J; Fung, J. S.; Mracek, J.; LaPierre, R. R. Nanotechnology 2010, **21**, 134018.

[45] Dayeh, S. A. Semicond. Sci. Technol. 2010, **25**, 024004.

[46] Van Tilburg, J. W. W.; Algra, R. E.; Immink, W. G. G.; Verheijen, M.; Bakkers, E. P. A. M.; Kouwenhoven, L. P. Semicond. Sci. Technol. 2010, **25**, 024011.

[47] Nag, B. R. Electron Transport in Compound Semiconductors, Springer-Verlag, 1980.

[48] Madelung, O. Physics of III-V Compounds, John Wiley and Sons, 1964.

[49] Wieder, H. H. Appl. Phys. Lett. 1974, **25**, 206-208.

[50] Watkins, S. P.; Tran, C. A.; Ares, R.; Soerensen, G. Appl. Phys. Lett. 1995, **66**, 882-884.

[51] Schrieffer, J. R. Phys. Rev. 1955, **97**, 641.

[52] Affentauschegg, C.; Wieder, H. H. Semicond. Sci. Technol. 2001, **16**, 708-714.

[53] Salfi, J.; Savelyev, I. G.; Blumin, M.; Nair, S. V.; Ruda, H. E. Nature Nanotechnology 2010, **5**, 737-741.

[54] H. Bruus, K. Flensberg, and H. Smith, "Magnetoconductivity of quantum wires with elastic and inelastic scattering," *Phys. Rev. B*, vol. 48, pp. 11144–11155, Oct 1993.

[55] K. Das and A. Mizel, "Radial dependence of the carrier mobility in semiconductor nanowires," *Journal of Physics: Condensed Matter*, vol. 17, no. 42, p. 6675, 2005.

[56] M. H. Evans, X.-G. Zhang, J. D. Joannopoulos, and S. T. Pantelides, "First-Principles Mobility Calculations and Atomic-Scale Interface Roughness in Nanoscale Structures," *Physical Review Letters*, vol. 95, p. 106802, Sept. 2005.

[57] S. Datta, *Quantum transport: atom to transistor; 2nd ed.* Cambridge: Cambridge Univ., 2005.

[58] D. K. Ferry and S. M. Goodnick, *Transport in nanostructures.* Cambridge Stud. Semicond. Phys. Micro Electr. Eng., Cambridge: Cambridge Univ. Press, 1997.

[59] A. Konar and D. Jena, "Tailoring the carrier mobility of semiconductor nanowires by remote dielectrics," *Journal of Applied Physics*, vol. 102, p. 123705, Dec. 2007.

[60] J. Wallentin, M. Ek, L. Wallenberg, L. Samuelson, and M. Borgstrom, "Electron trapping in inp nanowire fets with stacking faults," *Nano letters*, vol. 12, no. 1, pp. 151–155, 2011.

[61] P. Ebert, C. Domke, and K. Urban, "Direct observation of electrical charges at dislocations in gaas by cross-sectional scanning tunneling microscopy," *Applied Physics Letters*, vol. 78, no. 4, pp. 480–482, 2001.

[62] J. Salfi, S. V. Nair, I. G. Savelyev, M. Blumin, and H. E. Ruda, "Evidence for nonlinear screening and enhancement of scattering by a single coulomb impurity for dielectrically confined electrons in inas nanowires," *Phys. Rev. B*, vol. 85, p. 235316, Jun 2012.

[63] E. Rashba, "Electron spin operation by electric fields: spin dynamics and spin injection," *Physica E: Low-dimensional Systems and Nanostructures*, vol. 20, no. 3, pp. 189–195, 2004.

[64] S. Nadj-Perge, *Single Spins in Semiconductor Nanowires*. PhD thesis, Delft University of Technology, 2010.

[65] M. Koguchi, H. Kakibayashi, M. Yazawa, K. Hiruma, and T. Katsuyama, "Crystal structure change of gaas and inas whiskers from zinc-blende to wurtzite type," *Japanese Journal of Applied Physics*, vol. 31, no. Part 1, No. 7, pp. 2061–2065, 1992.

[66] G. Burkard, D. Loss, D. P. DiVincenzo, and J. A. Smolin, "Physical optimization of quantum error correction circuits," *Phys. Rev. B*, vol. 60, pp. 11404–11416, Oct 1999.

[67] X. Hu and S. Das Sarma, "Hilbert-space structure of a solid-state quantum computer: Two-electron states of a double-quantum-dot artificial molecule," *Phys. Rev. A*, vol. 61, p. 062301, May 2000.

[68] J. Schliemann, D. Loss, and A. H. MacDonald, "Double-occupancy errors, adiabaticity, and entanglement of spin qubits in quantum dots," *Phys. Rev. B*, vol. 63, p. 085311, Feb 2001.

[69] M. P. Nowak and B. Szafran, "Time-dependent configuration-interaction simulations of spin swap in spin-orbit-coupled double quantum dots," *Phys. Rev. B*, vol. 82, p. 165316, Oct 2010.

[70] K. Suzuki and R. Okamoto, "Effective operators in time-independent approach," *Progress of Theoretical Physics*, vol. 93, no. 5, pp. 905–917, 1995.

[71] I. d. P. R. Moreira, N. Suaud, N. Guihéry, J. P. Malrieu, R. Caballol, J. M. Bofill, and F. Illas, "Derivation of spin hamiltonians from the exact hamiltonian: Application to systems with two unpaired electrons per magnetic site," *Phys. Rev. B*, vol. 66, p. 134430, Oct 2002.

[72] V. Hurtubise, K.F. Freed, "The Algebra of Effective Hamiltonians and Operators: Exact Operators," *Advances in Chemical Physics*, p. 465–541, 2007.

[73] C. K. Duan and M. F. Reid, "Non-Hermitian perturbative effective operators: Connectivity and derivation of diagrammatic representation," *Jouranal of Chemical Physics*, vol. 115, pp. 8279–8284, Nov. 2001.

[74] A. R. Bryson and M. F. Reid, "Transition amplitude calculations for one- and two-photon absorption," *Journal of Alloys and Compounds*, vol. 275277, no. 0, pp. 284 – 287, 1998.

[75] M. F. Reid, C.-K. Duan, and H. Zhou, "Crystalfield parameters from ab initio calculations," *Journal of Alloys and Compounds*, vol. 488, no. 2, pp. 591 – 594, 2009. ¡ce:title¿Proceedings of the 25th Rare Earth Research Conference, June 22-26, Tuscaloosa, Alabama, USA¡/ce:title¿.

[76] R. Maurice, R. Bastardis, C. d. Graaf, N. Suaud, T. Mallah, and N. Guihery, "Universal theoretical approach to extract anisotropic spin hamiltonians," *Journal of Chemical Theory and Computation*, vol. 5, no. 11, pp. 2977–2984, 2009.

[77] S. Bednarek, B. Szafran, T. Chwiej, and J. Adamowski, "Effective interaction for charge carriers confined in quasi-one-dimensional nanostructures," *Physical Review B*, vol. 68, no. 4, p. 045328, 2003.

[78] R. Winkler, "Quasi-degenerate perturbation theory," *Spin–Orbit Coupling Effects in Two-Dimensional Electron and Hole Systems*, pp. 201–206, 2003.

[79] C. Bloch, "Sur la thorie des perturbations des tats lis," *Nuclear Physics*, vol. 6, no. 0, pp. 329 – 347, 1958.

[80] J. des Cloizeaux, "Extension d'une formule de lagrange des problmes de valeurs propres," *Nuclear Physics*, vol. 20, no. 0, pp. 321 – 346, 1960.

[81] J. Pedersen, C. Flindt, N. A. Mortensen, and A.-P. Jauho, "Failure of standard approximations of the exchange coupling in nanostructures," *Phys. Rev. B*, vol. 76, p. 125323, Sep 2007.

[82] M. J. Calderón, B. Koiller, and S. Das Sarma, "Exchange coupling in semiconductor nanostructures: Validity and limitations of the heitler-london approach," *Phys. Rev. B*, vol. 74, p. 045310, Jul 2006.

[83] A. Moroz and C. Barnes, "Spin-orbit interaction as a source of spectral and transport properties in quasi-one-dimensional systems," *Physical Review B*, vol. 61, no. 4, pp. 2464–2467, 2000.

[84] C. Flindt, A. Sørensen, and K. Flensberg, "Spin-orbit induced spin-qubit control in nanowires," in *Journal of Physics: Conference Series*, vol. 61, p. 302, IOP Publishing, 2007.

[85] L. H. Kristinsdóttir, J. C. Cremon, H. A. Nilsson, H. Q. Xu, L. Samuelson, H. Linke, A. Wacker, and S. M. Reimann, "Signatures of wigner localization in epitaxially grown nanowires," *Phys. Rev. B*, vol. 83, p. 041101, Jan 2011.

[86] T. Sand-Jespersen, J. Paaske, B. Andersen, K. Grove-Rasmussen, H. Jørgensen, M. Aagesen, C. Sørensen, P. Lindelof, K. Flensberg, and J. Nygård, "Kondo-enhanced andreev tunneling in inas nanowire quantum dots," *Physical review letters*, vol. 99, no. 12, p. 126603, 2007.

[87] V. Mourik, K. Zuo, S. Frolov, S. Plissard, E. Bakkers, and L. Kouwenhoven, "Signatures of majorana fermions in hybrid superconductor-semiconductor nanowire devices," *Science*, vol. 336, no. 6084, pp. 1003–1007, 2012.

[88] J. Bao, D. Bell, F. Capasso, N. Erdman, D. Wei, L. Fröberg, T. Mårtensson, and L. Samuelson, "Nanowire-induced wurtzite inas thin film on zinc-blende inas substrate," *Advanced Materials*, vol. 21, no. 36, pp. 3654–3658, 2009.